PHYSICAL REVIEW C VOLUME 44, NUMBER 2 AUGUST 1991

Charged-particle evaporation from hot composite nuclei: Evidence over a broad Z range for distortions from cold nuclear profiles

Winifred E. Parker,$^{(1),*}$ Morton Kaplan,$^{(1)}$ David J. Moses,$^{(1)}$ Giovanni La Rana,$^{(1),\dagger}$ Douglas Logan,$^{(2),\ddagger}$
Roy Lacey,$^{(3),\S}$ John M. Alexander,$^{(3)}$ Dalva M. de Castro Rizzo,$^{(3)}$ Paul DeYoung,$^{(4),**}$ Robert J. Welberry,$^{(1)}$
and John T. Boger$^{(3)}$
$^{(1)}$*Department of Chemistry, Carnegie Mellon University, Pittsburgh, Pennsylvania 15213*
$^{(2)}$*Lawrence Berkeley Laboratory, Berkeley, California 94720*
$^{(3)}$*Department of Chemistry, State University of New York at Stony Brook, Stony Brook, New York 11794*
$^{(4)}$*Department of Physics, State University of New York at Stony Brook, Stony Brook, New York 11794*
(Received 1 October 1990)

Charged-particle emission has been studied in ten heavy-ion reactions spanning composite systems of $16 \le Z \le 64$. By means of reversed kinematics, high-quality energy spectra were obtained for proton and alpha evaporation from compound nuclei with temperatures ~ 1.5–3.5 MeV and spins up to $\sim 70\hbar$. In some cases, deuteron and triton spectra were recorded as well. Statistical model calculations for spherical nuclei require systematically low emission barriers to reproduce the data. For the lighter systems, the effective spins (or moments of inertia) must be modified as well, whereas for the heavier systems this effect is of less importance. The roles of multistep particle emission and competition in the model calculations are assessed and found to be inadequate to explain the observed discrepancies. Calculations that model statically deformed nuclear emitters suggest that large deformations may be present, but they do not give a satisfactory overall picture. The very low proton energies in particular seem to indicate an extended density profile. Such an effect, together with the requirements for cluster preformation, may explain the observed low barriers for ^{1}H/^{4}He and the increasing mean energies found for the series ^{1}H, ^{2}H, ^{3}H, respectively.

I. INTRODUCTION

There is currently considerable interest in the evolution of nuclear properties and behavior as increasingly larger amounts of energy and angular momentum are introduced, and in determining the limits, of excitation energy and angular momentum that a nucleus can contain. Studies probing such phenomena are presently being pursued in three energy domains: (a) the region of temperature $T < 5$–7 MeV, where composite nuclei are held together by their mean field; (b) the intermediate-energy region of $7 \le T \le 20$ MeV, where unbound nucleonic clusters may briefly exchange energy before shattering; and (c) the relativistic-energy region, where subnucleonic particles may be instantaneously deconfined. Although the lower-energy domain has been studied for many years, a clear picture has not yet emerged for the variation of nuclear size and shape with temperature and spin. Gamma-ray spectroscopy has provided a wealth of information about cold nuclei near the yrast line, but it is in the continuum spectra of particles, fragments, and photons that one must search out the properties of nuclei with $T > 1$ MeV.

A variety of heavy-ion experiments in the low-energy regime have demonstrated that the composite nuclear systems produced often exhibit a high degree of thermal equilibration [1–30]. For reactions which proceed with such energy thermalization, the deexcitation properties of the hot, rotating nuclei may be elucidated with guidance from the well-developed framework of statistical model theory [31–33]. Measured energy spectra and angular distributions of evaporative light charged particles can be especially informative since they reflect properties of the nuclear system at the scission point. The low-energy parts of these spectra are dominated by effective emission barriers which arise, in turn, from the nuclear shape and size. The spectra slopes at high energies are determined primarily by the nuclear temperatures, with some influence from spin. The particle angular distributions are driven by the ratio of rotational energy to temperature, as represented [33,34] by the parameter β_2:

$$\beta_2 = \frac{\hbar^2 J^2}{2\mathcal{J}T}\left[\frac{\mu R^2}{\mathcal{J}+\mu R^2}\right], \tag{1}$$

where J is the spin of the emitter, and $\mathcal{J}$ and T denote the moment of inertia and temperature, respectively, of the daughter nucleus. Hence it is apparent that both the energy spectra and the angular distributions are needed in the search for a consistent interpretation of the roles of shape, temperature, and spin.

Particle evaporation spectra and angular distributions of especially good quality can be obtained for reactions carried out in reversed kinematics [35]. For incident energies of $E/A \sim 8.5$ MeV or lower, full momentum transfer and energy equilibration generally provide the dominant path to composite-nucleus formation. This situation leads to a straightforward characterization of the initial charge, energy, and spin of the emitting nuclei. In this paper we report the results of measurements for ten heavy-ion reactions, all but one in reversed kinematics. Composite nuclei with Z between 16 and 64 have been produced with temperatures $T \sim 1.5-3.5$ MeV and spins up to $J \sim 70\hbar$.

In the following sections, we first give a general description of the experiments, emphasizing those aspects which are particularly important for obtaining high-quality energy spectra of emitted charged particles. We then present the evidence which guides us in attributing the observed ^{1}H/^{4}He particles to evaporation from reasonably well-characterized and equilibrated emitters. This is followed by detailed comparisons between the measured alpha and proton data and statistical model predictions for their evaporative energy spectra and angular distributions. The calculations were carried out several times using different assumptions regarding the characteristics of the excited composite nuclei. Finally, we discuss the significance of the agreements and disagreements between experiment and theory, and draw conclusions which seem to apply generally to the broad range of systems investigated.

As the data and results presented here are derived from our own experiments, we are confident that the methods of analysis, constraints, and comparisons with theoretical calculations have been applied in a consistent manner for all the reactions. At a future time we may present the results of a similar systematic analysis of alpha- and proton-evaporation spectra, using a much larger, but less controlled, experimental database from the published literature [36].

II. EXPERIMENTAL PROCEDURES

As the major objectives of this study involve detailed comparisons of observed charged-particle emission with theoretical calculations, it was of utmost importance that the measurements include the low-energy parts of the spectra as well as the high-energy tails. Operationally, this required that the effective detector thresholds be substantially lower than the most probable particle energies. Using very heavy-ion beams in reversed kinematics [35], the large center-of-mass velocities served as a booster which greatly increased the particle energies in the forward hemisphere. This feature, together with the use of relatively-low-threshold detector systems, often permitted recording the particle spectra down to very low c.m. emission energies.

In addition to the enhancement of particle energies, reversed kinematics produces an interchange of forward and backward c.m. hemispheres, as observed in the laboratory [35]. Hence the purely evaporative emission from the composite system, which is most readily observed in the backward hemisphere under normal kinematics [37,38], is projected into the forward hemisphere (under reversed kinematics) where the low-energy-detection capabilities are also maximized. Correspondingly, direct or prethermalization particle emission tends to appear in the backward hemisphere, i.e., the c.m. direction of the lighter reaction partner.

The experiments were carried out at the Lawrence Berkeley Laboratory, where the SuperHILAC accelerator provided intense beams of ^{20}Ne, ^{40}Ar, ^{56}Fe, ^{86}Kr, ^{109}Ag, and ^{121}Sb ions. These projectiles were used to bombard self-supporting targets of C (150–200 μg/cm^2) and Al (400 or 1900 μg/cm^2). We summarize in Table I the characteristics of the various reactions studied. For convenience in later discussions, we have numbered the reactions as indicated in the first column of the table. Column 2 shows the reaction system, which produces the composite nucleus listed in column 3. Columns 4 and 5 give the initial atomic number (Z_{CN}) and the initial total excitation energy ($E_{\text{c.m.}}+Q$) of the composite nucleus.

The light charged particles ^{1}H and ^{4}He (and sometimes ^{2}H and ^{3}H as well) were measured either in three-element Si telescopes (50 μm, 500 μm, 5000 μm) or in gas-ionization (Wedge) telescopes as described elsewhere [39,40]. The detectors were protected from low-energy electrons and photons by thin Pb or Au covers foils. Energy calibrations were made with alpha-emitting sources of ^{148}Gd (3.18 MeV), ^{241}Am (5.45 MeV), and ^{212}Pb (6.05 and 8.78 MeV), and solid angles were determined by counting the alpha emissions from ^{148}Gd and ^{241}Am sources of known disintegration rate at the target position. The particle spectra were generally recorded at a number of laboratory angles, in order to characterize the c.m. angular distributions and allow extraction of the β_2 parameters [see Eq. (1)] from the data. If we assume (for illustrative purposes) that β_2 has a unique value for a

TABLE I. Characteristics of the reactions studied in the present work.

No.	System	Composite nucleus	Z_{CN}	($E_{\text{c.m.}}+Q$) (MeV)
1	167-MeV ^{20}Ne+^{12}C	^{32}S	16	81
2	167-MeV ^{20}Ne+^{27}Al	^{47}V	23	114
3	340-MeV ^{40}Ar+^{12}C	^{52}Cr	24	99
4	190-MeV ^{40}Ar+^{27}Al	^{67}Ga	31	91
5	476-MeV ^{56}Fe+^{12}C	^{68}Ge	32	91
6	730-MeV ^{86}Kr+^{12}C	^{98}Mo	42	92
7	956-MeV ^{109}Ag+^{12}C	^{121}I	53	92
8	1030-MeV ^{121}Sb+^{12}C	^{133}La	57	89
9	956-MeV ^{109}Ag+^{27}Al	^{136}Nd	60	163
10	1030-MeV ^{121}Sb+^{27}Al	^{148}Gd	64	157

given emission, then the angular distribution is given by the relationship [34]

$$W(\theta)\propto \exp(-\tfrac{1}{2}\beta_2\sin^2\theta)I_0(\tfrac{1}{2}\beta_2\sin^2\theta)\ , \qquad (2)$$

where $W(\theta)$ is the inclusive particle intensity at c.m. angle θ with respect to the beam direction, and $I_0(x)$ is a zero-order Bessel function of argument x. In practice, a more complete calculation was used that includes a distribution of spin values. Most of the results presented below are derived from inclusive data. However, for several reactions we also measured the heavy reaction fragments in coincidence with light charged particles, using for this purpose either gas-ionization telescopes [41] or a large position-sensitive avalanche detector backed by an ionization chamber. The heavy-fragment coincidence data served as a useful tool in identifying and comparing several possible sources of charged-particle emission. As discussed below, evaporation from the composite nucleus is the dominant source of the observed particles for the reactions studied here.

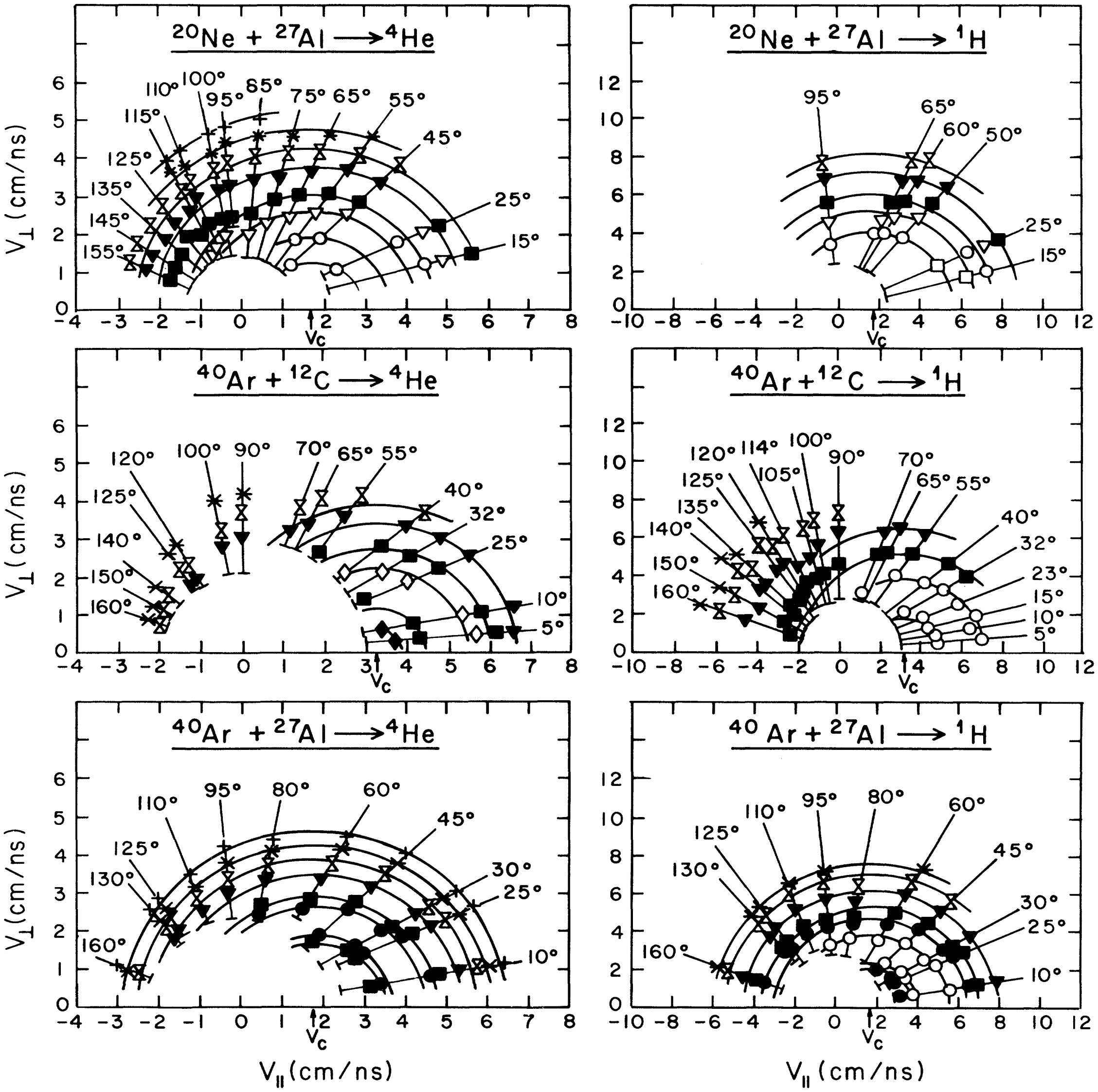

FIG. 1. Contour maps of the invariant cross section $(d^2\sigma/d\Omega\, dE)p^{-1}c^{-1}$ in units of mb/sr MeV^2 for three representative lighter-mass systems as indicated. For each reaction, the ^{4}He data are on the left, and the ^{1}H data are on the right. The axes $V_{\parallel}$ and $V_{\perp}$ denote laboratory velocity components parallel and perpendicular to the beam, respectively. The circular arcs are centered on V_c (see arrows), the velocity of the center of mass. Straight lines are drawn along the laboratory angles and terminated at the detector thresholds. The invariant cross section magnitudes are □: 3×10^{-1}; ○: 1×10^{-1}; △: 5×10^{-2}; ◇: 4×10^{-2}; ▽: 3×10^{-2}; ●: 2×10^{-2}; ■: 1×10^{-2}; ▲: 5×10^{-3}; ◆: 4×10^{-3}; ▼: 1×10^{-3}; X: 1×10^{-4}; *: 1×10^{-5}; +: 1×10^{-6}.

III. RESULTS AND DISCUSSION

A. Evidence for the dominance of ^{1}H/^{4}He evaporation from the composite systems

Our objective is the interpretation of particle evaporation spectra and angular distributions in terms of the characteristics of the emitters. This is accomplished by comparisons of the data with the predictions of statistical model theory. Therefore, it is important to identify the dominant emission sources.

Velocity-contour maps of the invariant (particle) cross section, $[(d^2\sigma/d\Omega\, d\varepsilon)p^{-1}c^{-1}]_{\rm lab}$, provide a picture of the overall reaction pattern. We have constructed such maps from the ^{1}H and ^{4}He data for each of the reactions listed in Table I, a total of 20 maps. We show in Fig. 1 several sets of these maps. These are representative of the lighter-mass systems. (Others have been published elsewhere [35].) The left side of Fig. 1 gives the ^{4}He data, with the corresponding ^{1}H data on the right. The first reaction shown (reaction 2, ^{20}Ne+^{27}Al) is in normal kinematics, and the other reactions are in reversed kinematics. The circular arcs are centered on the velocity of the center of mass (as indicated in Fig. 1), and represent the emission patterns to be expected from isotropic evaporative sources moving with this velocity. As shown in Fig. 1, the circles describe the bulk of the data rather well. Particles from direct reactions or prethermalization emission would manifest themselves as strong deviations from the circles in the direction of the light reaction partner, i.e., forward for normal kinematics and backward for reversed kinematics. Such deviations are clearly seen in the forward-angle data for the ^{20}Ne+^{27}Al reaction, and in the backward-angle data for the two ^{40}Ar-induced reactions in Fig. 1. Much smaller deviations from the circles are also detected in the direction of the heavy reaction partner; these are attributable to spin-driven angular anisotropies in evaporative decay (see, for example, Ref. [22]).

Figure 2 gives the measured angular distributions, transformed to the c.m. systems, for the three reactions described in Fig. 1. We show in Fig. 2 the angular regions which Fig. 1 indicates are dominated by essentially pure evaporative emission, typically the (c.m.) hemisphere in the direction of the heavy reactant. The curves in Fig. 2 are the results of statistical model calculations and will be described in Sec. III B, below.

In Fig. 3, we present several invariant cross-section maps for ^{4}He and ^{1}H from reactions 6, 8, and 10, representative of the heavier-mass systems in Table I. We see here the same general features noted in Fig. 1, namely, very good agreement in the forward directions (reversed kinematics) with the circular arcs centered on the c.m. velocity, and rather large deviations from the circles in the more backward (light partner) directions. The corresponding cross-section maps for the ^{109}Ag-induced reactions, 7 and 9 in Table I, are very similar to the corresponding ^{121}Sb-induced reactions, 8 and 10. Because of the stronger reversed kinematics, and the resulting larger center-of-mass velocities, the data in Fig. 3 are shifted forward along the beam direction, compared to Fig. 1. For the ^{121}Sb+^{12}C system, the most strongly reversed-kinematics reaction in Table I, the deviations from the circular arcs are apparent at sideways angles (50°, 60°, 80° for ^{4}He, and 80° for ^{1}H); however, these laboratory angles are, in fact, backward angles in the c.m. system of the reaction.

The c.m. angular distributions for the three reactions in Fig. 3 are displayed in Fig. 4. As was the case for the ligher-mass systems in Fig. 2, we find that the c.m. angular distributions of ^{1}H and ^{4}He, in the regions of evaporative emission, are gently increasing functions of angle in the direction of the heavy reaction partner, as expected. The statistical model calculations, shown as curves in

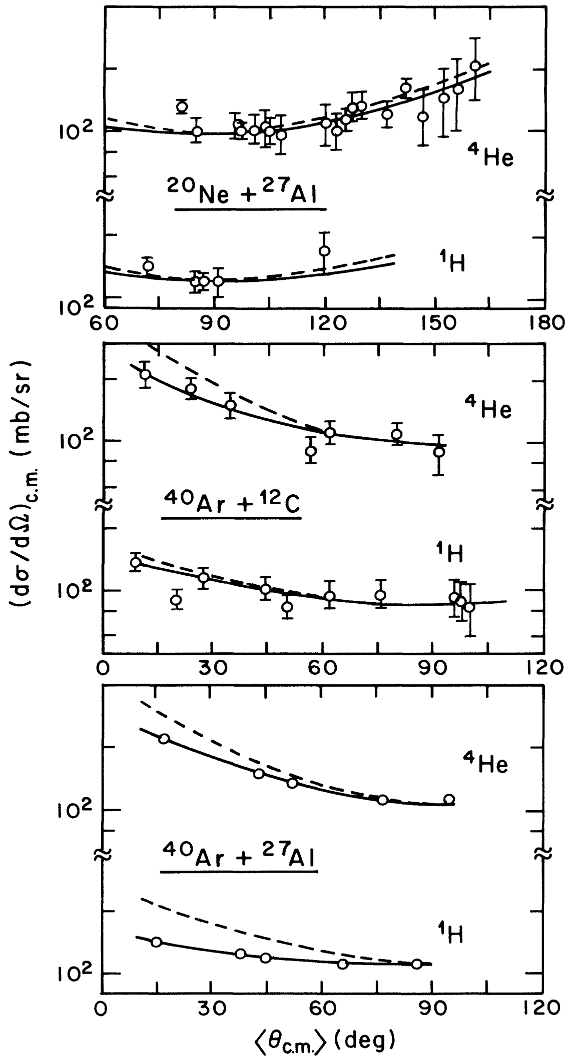

FIG. 2. Angular distributions of ^{4}He and ^{1}H in the c.m. system, for the three reactions in Fig. 1. The points are experimental data and the curves are statistical model calculations for spherical nuclei using constrained parameters (— — —) and fitted parameters (——). See text and Table II. The calculated curves have been normalized to the data at 90° to illustrate the differences in anisotropies.

Fig. 4, will be discussed in the next section.

We have seen from the discussions of Figs. 1–4 that each of the reactions in Table I exhibits an angular region where the ^{1}H/^{4}He emission appears to be dominated by evaporation from the composite nuclei. Let us now consider the possibilities for interfering emissions from other sources, and what information we can bring to bear on estimating the relative magnitudes involved. In the relevant angular regions, the angular distributions of ^{1}H and ^{4}He, as well as their energy distributions (from the maps in Figs. 1 and 3, and the energy spectra themselves, to be presented later) have shapes which are characteristic of evaporation from thermally equilibrated composite nuclear systems. For those reactions which lead to binary decay of the composite system (e.g., fission, or deeply inelastic processes), evaporation from reaction fragments is a likely source of ^{1}H/^{4}He particle emissions, which could be mixed with that from the composite-system evaporation (CE).

The first six reactions in Table I yield composite systems for which fission is essentially negligible. For these reactions, only evaporation from projectile-like fragments (or target-like, in the case of reaction 2) could seriously affect our analysis of the ^{1}H/^{4}He data. In the case of 190-MeV ^{40}Ar+^{27}Al (reaction 4), we used a position-sensitive avalanche detector backed by an ionization chamber in order to measure evaporation residues and projectile-like fragments in coincidence with light charged particles. This was done to estimate the charged-particle multiplicities associated with each process. At this energy, less than 1% of the ^{1}H/^{4}He arises from reactions with projectile-like survivors, and hence

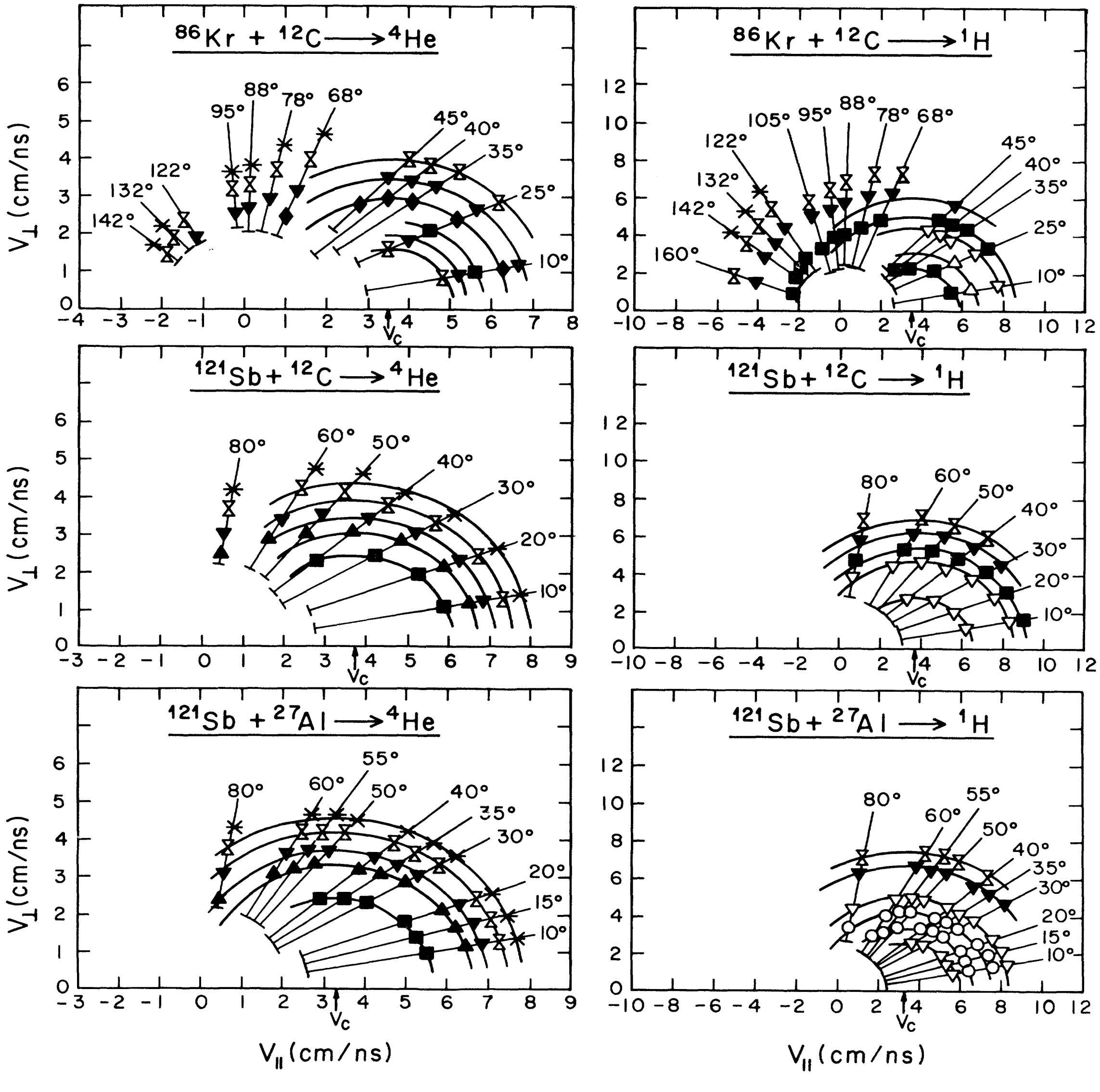

FIG. 3. Invariant cross-section maps as in Fig. 1, but for three heavier-mass systems as indicated. The notation and symbols are as in Fig. 1.

the forward-angle inclusive ^{1}H/^{4}He data presented here are not biased by emissions from such fragments. In a similar manner, Ikezoe *et al.* [42] have studied the reactions of 160-MeV ^{16}O+^{27}Al, and determined that essentially all of the evaporative ^{1}H/^{4}He is associated with evaporation-residue formation from fusion reactions. As this ^{16}O-induced reaction is quite close in energy and type to our reaction 2 (167-MeV ^{20}Ne+^{27}Al), we feel that a corresponding conclusion is valid for the ^{20}Ne-induced reaction also. The heavy fragment coincidence data just described are consistent with our observations that the ^{1}H/^{4}He data in Fig. 1 show no deviations from CE origins in the relevant angular regions. The inclusive evaporation-residue (ER) measurements of Morgenstern *et al.* [43], for the ^{20}Ne+^{27}Al reaction, also indicate the dominance of ER particle evaporation at the energy considered here. As projectile velocities are significantly greater than the c.m. velocities, the emission patterns would be appreciably perturbed if ^{1}H/^{4}He evaporation from projectile-like fragments were substantial. As such effects are not visible in any of the invariant cross-section maps, it is reasonable to assume that evaporation from projectile-like fragments must be quite small in comparison to the dominant CE processes. (This point shall be discussed further in Sec. III B.)

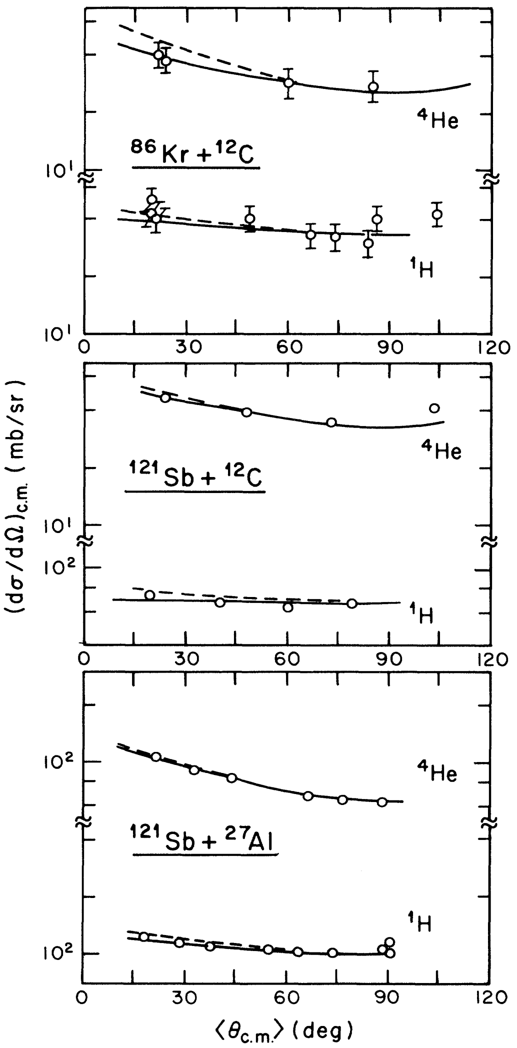

FIG. 4. Center-of-mass angular distributions of ^{4}He and ^{1}H as in Fig. 2, but for the three reactions in Fig. 3. The notation and symbols are as in Fig. 2.

For the last four reactions in Table I, one might imagine that evaporation after binary fission is a plausible decay mode, along with that from evaporation residues and projectile-like survivors. We do have experimental data on this point. In the experiment involving reaction 10, 1030-MeV ^{121}Sb+^{27}Al, fission fragments and projectile-like fragments were measured in coincidence with ^{1}H/^{4}He particles. Also, particle-particle coincidences were measured in addition to the singles ^{1}H/^{4}He data. From the magnitudes of the various coincidence cross sections, compared to the particle inclusive cross sections, we infer that most of the particle-particle coincidences are associated with evaporation residues and only about 20% of the ^{4}He and 27% of the ^{1}H total (angle-integrated) cross sections can be attributed [44] to other evaporative sources (i.e., fission and projectile-like fragments). These emissions have distinctive energy spectra and kinematic energy shifts with angle, and their contributions to the observed spectra can be accounted for by means of a reaction simulation code [45].

A detailed study of the ^{40}Ar+$^{\text{nat}}$Ag system [22,23], which is quite similar to reactions 9 and 10 in Table I, provides further confidence that the dominant source of evaporative ^{1}H/^{4}He is the composite nucleus in these reactions. Although no direct measurements of fragment-particle coincidences have been made for reactions 7 and 8, we expect from systematics that the contributions resulting from fission and projectile-like fragments would be substantially smaller than in reactions 9 and 10.

The comparisons of ^{1}H/^{4}He data with statistical model calculations, to be described in the next section, are consistent with the arguments presented in this section, above, for all 10 reactions in Table I.

B. Comparisons of experimental ^{1}H/^{4}He energy spectra and angular distributions with statistical model calculations for spherical nuclei

Representative ^{1}H and ^{4}He energy spectra for the 10 reactions studied are shown in Figs. 5 and 6, along with some calculated curves to be discussed below. For each reaction, the spectra were selected from the laboratory angular regions where the velocity-contour (invariant cross-section) maps indicate dominance by essentially pure evaporative emission from the composite systems. Figure 5 gives spectra from reactions 1–5 (Table I), and those from reactions 6–10 are in Fig. 6. In each figure, the ^{4}He spectra are on the left, and the corresponding ^{1}H spectra (from the same reaction) are on the right. The laboratory angles where each spectrum was measured are indicated on the figures, and the corresponding c.m. angular distributions for these reactions are represented in Figs. 2 and 4, discussed above. As can be seen from Figs.

5 and 6, the laboratory energy spectra have characteristically evaporative shapes, modified by the kinematic shifts associated with the large center-of-mass motions in reversed-kinematic reactions. Note also that most of the spectra have been obtained with good statistical accuracy over a range well below the most probable energies, as well as on the high-energy slopes. These measured features provide important constraints in comparing the data with model calculations involving parameter choices.

We have carried out statistical model calculations [31–33] with different assumptions concerning the transition-state nuclei. In this section we consider spherical transition-state systems characterized by three quantities: (1) an effective emission barrier, (2) a spin distribution from zero to J_{cr}, and (3) a mean excitation energy

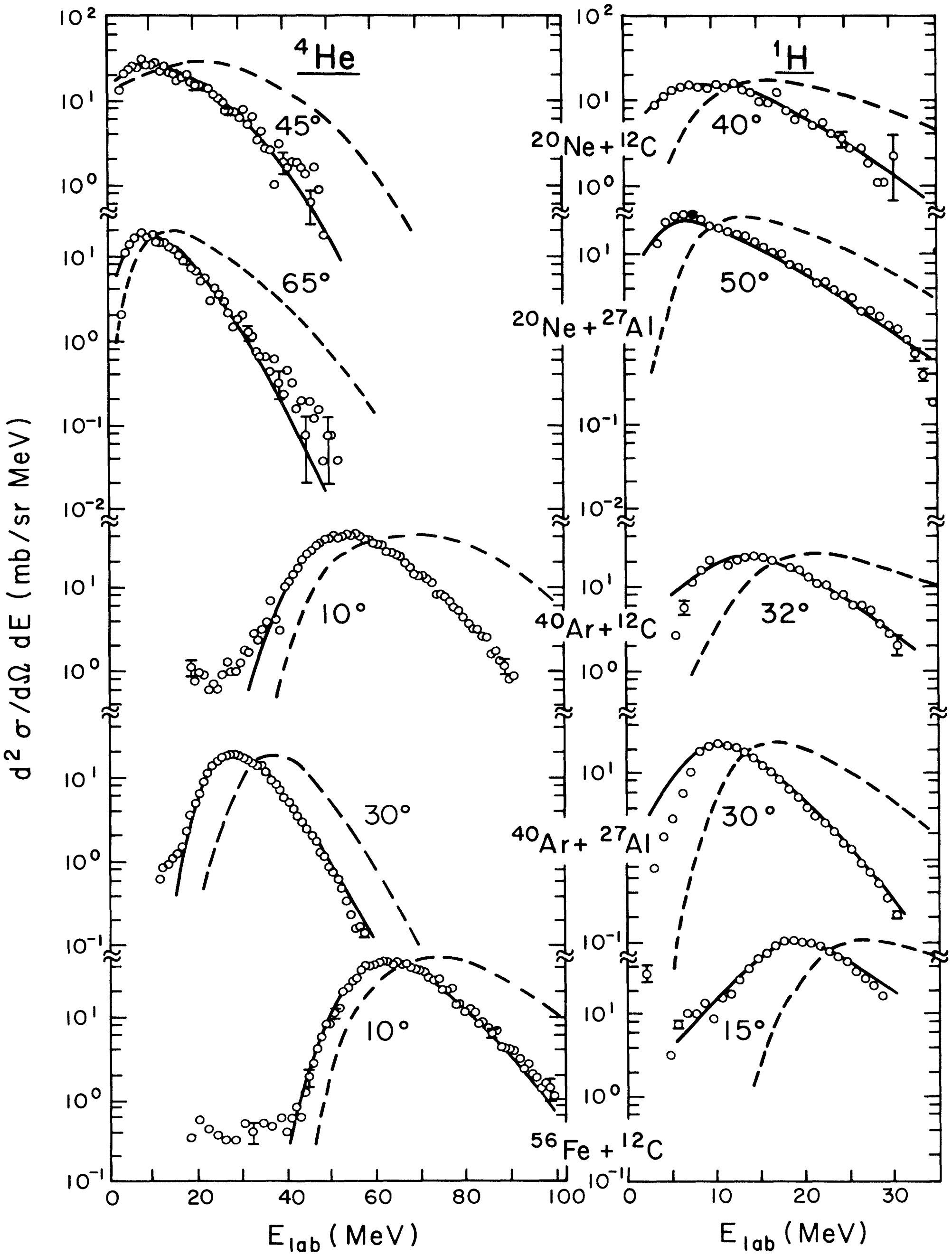

FIG. 5. Laboratory energy spectra of ^{4}He (left) and ^{1}H (right) for reactions 1–5 of Table I, as indicated. The points are experimental and the curves are results from statistical model calculations for spherical nuclei using constrained parameters (— — —) and fitted parameters (———). See text and Table II for details.

E^*. We shall later describe results for deformed nuclear systems. The calculations were performed using the well-documented evaporation-simulation code GANES [45]. This code evaluates the relative probability of emitting a particle of given mass, charge, energy, and orbital angular momentum from a nucleus with known mass, charge, excitation energy, and spin, into an angle whose direction is specified with respect to the emitter spin. Recoil effects and Jacobians associated with system transformations are taken into account on an event-by-event basis. Particle spectra and angular distributions are built by repeated Monte Carlo sampling of the relevant quantities, until the desired level of statistical significance is achieved.

For the first series of calculations, we have used triangular spin distributions in the entrance channels, with values of J_{cr} estimated for each reaction from appropriate fusion cross-section data [46]. The exit-channel emission barriers for ^{1}H and ^{4}He were taken from fusion barrier systematics [47] for the corresponding inverse reac-

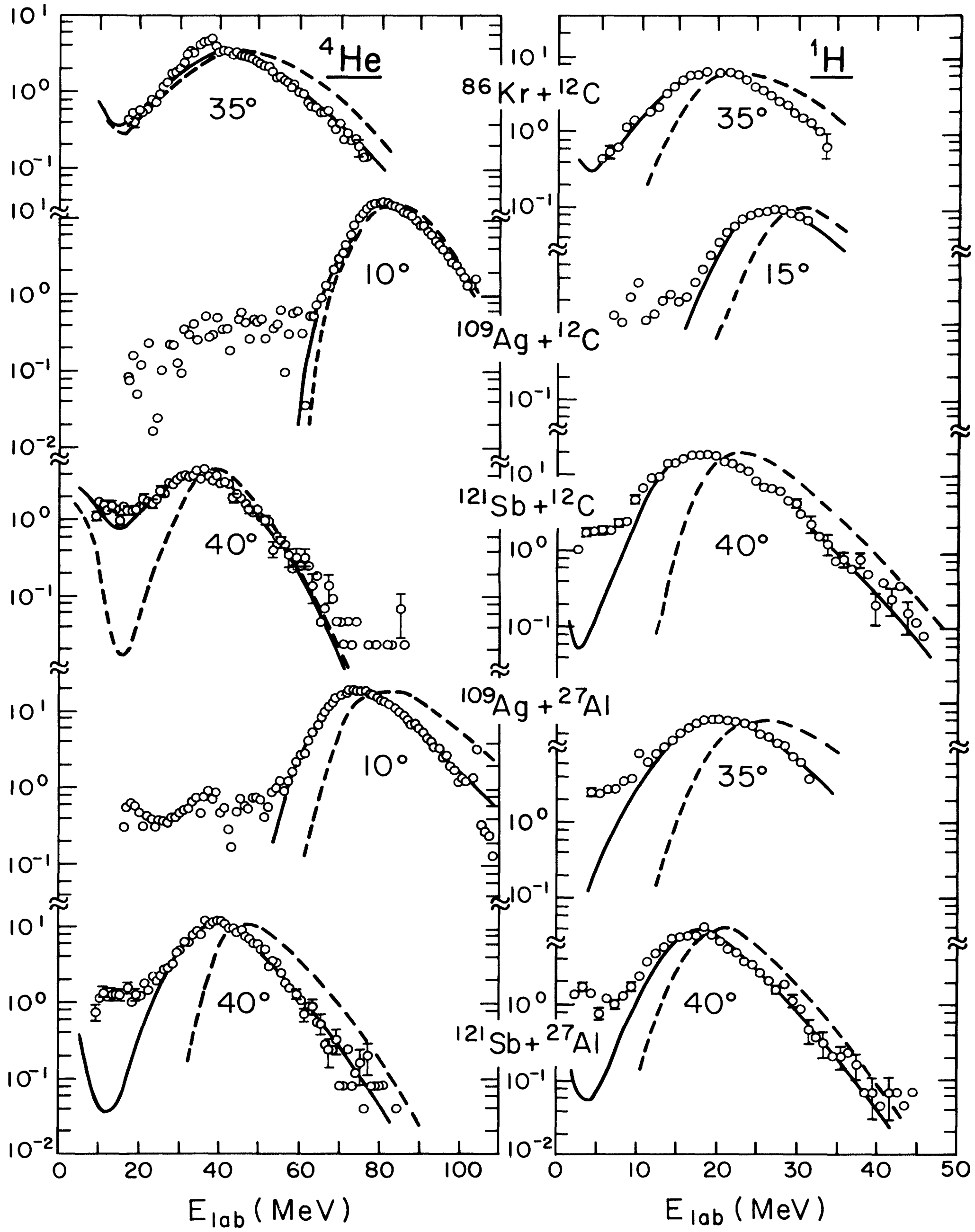

FIG. 6. Laboratory energy spectra of ^{4}He (left) and ^{1}H (right) as in Fig. 5, but for reactions 6–10 of Table I, as indicated. The symbolism is the same as in Fig. 5.

TABLE II. Properties of the ^{1}H/^{4}He evaporative emitters.

Emitted particle	Anisotropy parameter[a] β_2	Constrained parameters[b] $(E_{\text{c.m.}}+Q)$ (MeV)	J_{crit} ($\hbar$)	B_{fus} (MeV)	Z_{eff}[c]	Spherical fits[d] E^* (MeV)	J_{cr} ($\hbar$)	B (MeV)
167-MeV ^{20}Ne+^{12}C→^{32}S*								
^{1}H	0.4	81	22	3.4	15	56.7	10	0.7
^{4}He	1.4	81	22	4.6	15	56.7	10	4.5
167-MeV ^{20}Ne+^{27}Al→^{47}V*								
^{1}H	0.7	114	30	4.1	22	68.4	20	1.0
^{4}He	2.3	114	30	6.6	22	68.4	20	5.3
340-MeV ^{40}Ar+^{12}C→^{52}Cr*								
^{1}H	0.7	99	35	4.2	23	49.5	24	1.5
^{4}He	3.1	99	35	6.8	23	59.4	24	5.2
190-MeV ^{40}Ar+^{27}Al→^{67}Ga*								
^{1}H	0.8	91	46	4.9	29	45.5	30	2.0
^{4}He	3.1	91	46	8.4	29	54.6	30	7.3
476-MeV ^{56}Fe+^{12}C→^{68}Ge*								
^{1}H	0.7	91	39	5.0	30	45.5	27	2.5
^{4}He	2.2	91	39	8.7	30	54.6	27	7.3
730-MeV ^{86}Kr+^{12}C→^{98}Mo*								
^{1}H	0.3	92	48	6.3	42	78.2	37	4.5
^{4}He	1.4	92	48	11.5	42	87.4	37	11.2
956-MeV ^{109}Ag+^{12}C→^{121}I*								
^{1}H	0.3	92	39	7.4	52	55.2	39	5.4
^{4}He	1.3	92	39	13.9	52	55.2	39	13.0
1030-MeV ^{121}Sb+^{12}C→^{133}La*								
^{1}H	0.4	89	40	7.8	56	53.4	38	6.2
^{4}He	1.0	89	40	14.7	56	53.4	38	13.5
956-MeV ^{109}Ag+^{27}Al→^{136}Nd*								
^{1}H	0.4	163	67	8.1	59	97.8	62	5.0
^{4}He	1.5	163	67	15.5	59	97.8	62	12.0
1030-MeV ^{121}Sb+^{27}Al→^{148}Gd*								
^{1}H	0.5	157	65	8.6	63	94.2	65	5.5
^{4}He	1.5	157	65	16.3	63	94.2	65	13.0

[a] Anisotropy parameter [Eq. (1)] which characterizes the experimental angular distribution. The uncertainty in β_2 is ± 0.2.

[b] Parameter sets used to calculate energy spectra and angular distributions with an evaporation model for spherical nuclei. These parameters were not varied, and resulted in the dashed curves in Figs. 2, 4, 5, and 6. The quantity $(E_{\text{c.m.}}+Q)$ is the initial total excitation energy of the composite system, obtained from the relevant masses and the incident beam energy. J_{crit} is the maximum angular momentum in a triangular entrance-channel distribution, derived from the appropriate reaction cross section for evaporation-residue formation. B_{fus} is the fusion barrier for the inverse reaction, obtained from systematics [47]. These fusion barriers correspond to the emitter nucleus specified by Z_{eff} in column 6.

[c] Effective atomic number of the average nuclear emitter. These values were lowered from the Z of the composite system by small corrections of 0–2 Z units, based upon the observed effective excitation energies and average charged-particle multiplicities. For simplicity, we assumed here that ^{1}H and ^{4}He are each emitted in the average evaporation chain, and therefore arise from the same Z_{eff}. The effective mass numbers were scaled accordingly. These corrections have only small effects on the calculated results (see Fig. 12).

[d] Parameters derived by fitting the experimental energy spectra and angular distributions with an evaporation model for spherical nuclei. These parameters resulted in the solid curves in Figs. 2, 4, 5, and 6. E^* is the effective emitter excitation energy, J_{cr} is the maximum spin from a triangular distribution in the entrance channel, and B is the effective *s*-wave emission barrier. The estimated uncertainties are E^*, $\pm 10\%$; J_{cr}, $\pm 2\hbar$ for the ^{4}He data, except for reaction 9, where the uncertainty is $\pm 4\hbar$; for ^{1}H evaporation, the sensitivity to spin is relatively weak and the values of J_{cr} were chosen for consistency with the ^{4}He data; B, ± 0.5 MeV, except for ^{1}H from the ^{20}Ne-induced reactions (1 and 2), where the uncertainty is ± 0.8 MeV.

tions. With spherical moments of inertia and spins fixed by cross-section data, only the effective temperatures (corresponding to the mean excitation energies) can be adjusted in attempting to reproduce the experimental data. If we assume first-step emission, we obtain the results shown as dashed curves in Figs. 2 and 4 for the angular distributions and in Figs. 5 and 6 for the particle energy spectra. In comparison with the experimental data, the calculated energy spectra are much too energetic and the c.m. angular distributions are too anisotropic. If we relax the assumption of first-step emission by reducing the effective temperatures, the calculated angular distributions become even more anisotropic [see Eqs. (1) and (2)]. Clearly this takes us in the wrong direction.

In order to obtain satisfactory fits to the energy spectra and angular distributions, we repeated the Monte Carlo calculations, this time allowing three parameters to be varied: the effective J_{cr}, the mean initial excitation energy, and the effective particle evaporation barrier. The effects of modifying each of these parameters are as follows. Decreasing J_{cr} produces lower spinoff energies, thereby softening the high-energy tails of the energy spectra, and simultaneously decreasing the angular anisotropies. Lowering the mean initial excitation energies leads to lower spectral temperatures, and increases the anisotropy [see Eq. (1)]. Changing the emission barriers shifts the spectra in energy. The resulting fits to the experimental data are shown as the solid curves in Figs. 2, 4, 5, and 6. As can be seen, we are now able to achieve rather good fits to the energy spectra and angular distributions for both ^{4}He and ^{1}H in all of the reactions.

The results from our model calculations are given in

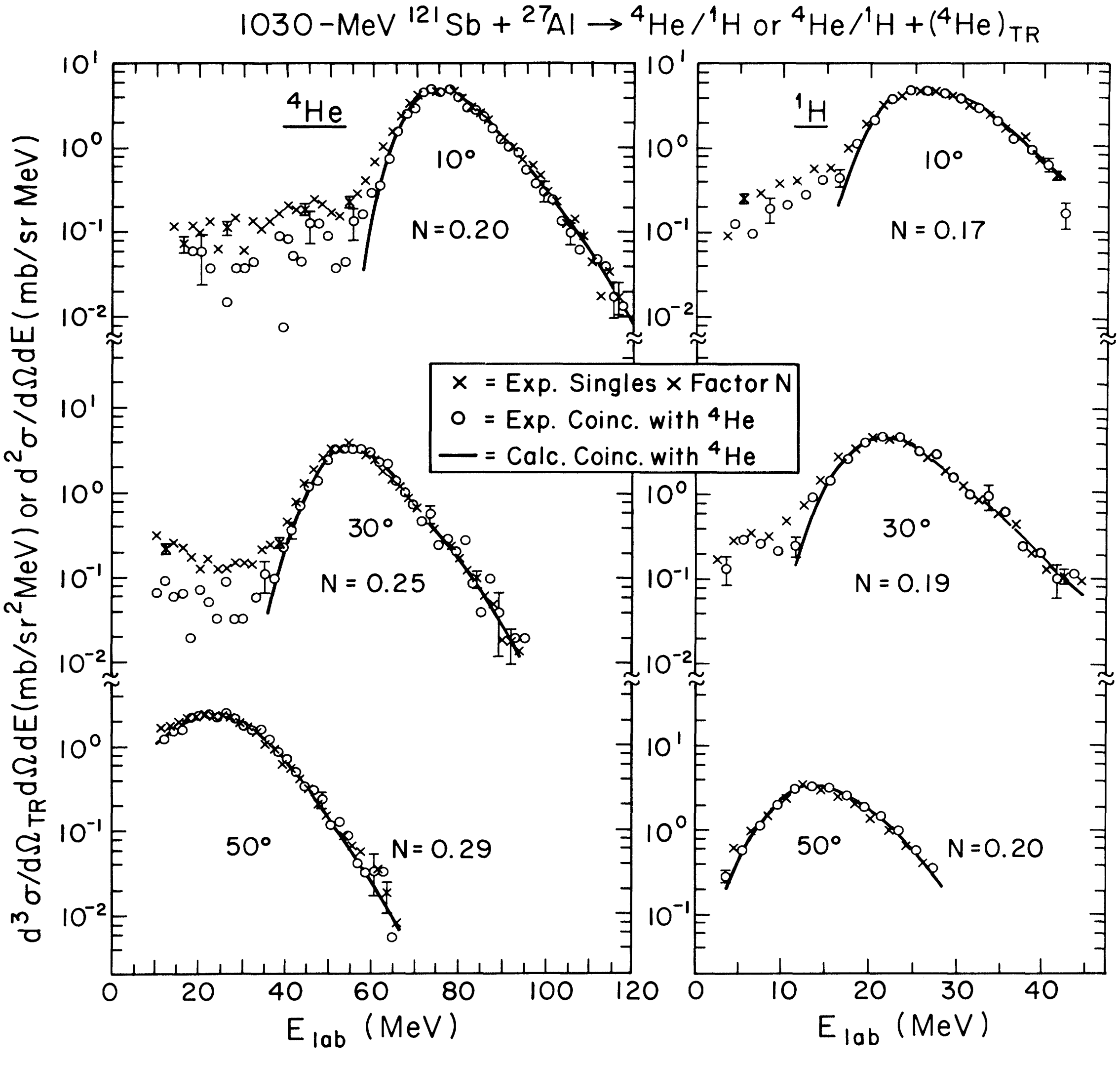

FIG. 7. Comparisons of ^{4}He (left) or ^{1}H (right) singles (inclusive) data with corresponding spectra gated (or triggered) by a coincident ^{4}He particle. The data shown are for reaction 10 (see Table I) at three laboratory angles as indicated. The solid curves are the results of statistical model calculations for the particle-particle coincidences, using the same set of parameters (see Table II) derived from the inclusive data.

Table II. The first column gives the emitted particle (^{1}H or ^{4}He), followed in column 2 by the value of β_2, which characterizes the experimental angular distribution. The next three columns summarize the "constrained parameters," namely ($E_{\text{c.m.}}+Q$), the total initial excitation energy of the composite system; J_{crit}, the sharp cutoff angular momentum estimated from fusion cross-section data [46]; and B_{fus}, the fusion barrier for the inverse reaction obtained from systematics [47]. These constrained parameter sets yielded the dashed curves in Figs. 2, 4, 5, and 6. Next we indicate the effective atomic number of the average emitter, estimated from the excitation energy loss and the charged-particle multiplicity. (The calculated results are rather insensitive to the exact value of Z_{eff}. See Fig. 12 later.) The last three columns in Table II give the "best-fit" parameters for the spherical nucleus model, and correspond to the solid curves for the various reactions shown in Figs. 2, 4, 5, and 6. E^* is the mean excita-

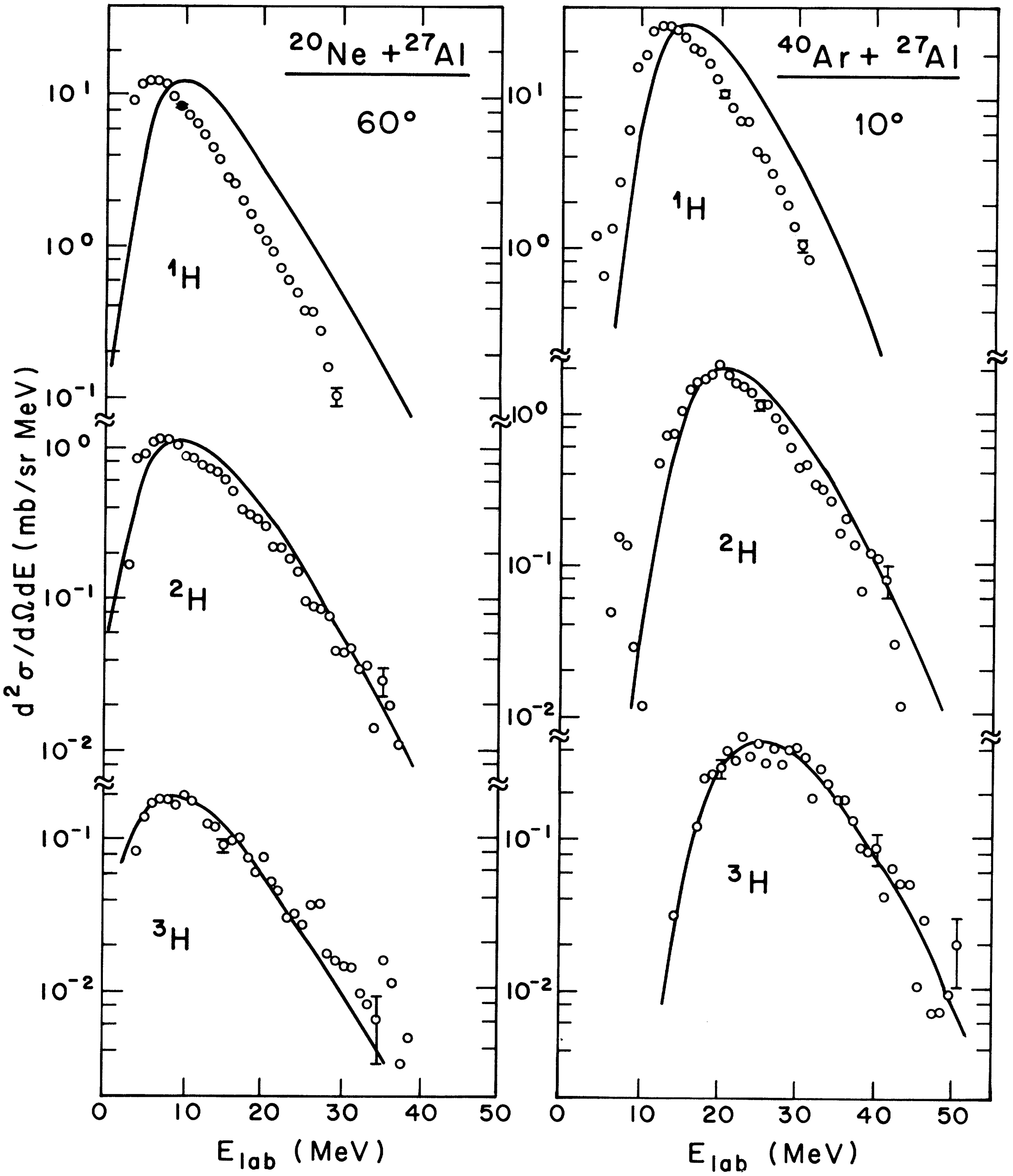

FIG. 8. Comparison of representative ^{1}H, ^{2}H, and ^{3}H energy spectra for two of the reactions studied, as indicated. The points are experimental data, and the solid curves were calculated from the statistical model using the constrained parameter sets from Table II. The barriers for ^{2}H and ^{3}H were taken as equal to that for ^{1}H in the same system.

tion energy of the emitter, J_{cr} is the maximum value of the spin from a triangular entrance-channel spin distribution, and B is the effective *s*-wave emission barrier. Comparing column 7 with column 3, we see that the derived values of E^* are lower in each case than the corresponding value for the initial compound nucleus. Since ^{1}H or ^{4}He emission can occur at any step of the evaporation cascade, it is reasonable to expect such excitation energy loss before the average emission step. Typically, the fits require $\sim 40\%$ of initial excitation energy loss, except for the ^{86}Kr$+^{12}$C reaction where the loss is $\sim 10\%$. Interestingly, the ^{86}Kr-induced reaction also has a much lower ^{1}H/^{4}He evaporative multiplicity [35], compared to the other reactions [35,48].

Table II often indicates reductions in emitter spins (or J_{cr}) when compared to J_{crit}, an effect which is demanded by the ^{4}He spectra and angular anisotropies. (One should note, however, that increasing the moment of inertia would produce the same effect as decreasing the emitter spin.) This is particularly important for ^{4}He emission in the lighter systems, where the moment of inertia of a small sphere accentuates the role of spin [49]. [See Eq. (1) and the experimental β_2 values in Table II.] For all systems, both ^{1}H and ^{4}He spectra require substantial lowering of the effective emission barriers, compared to the fusion barriers [47] shown in Table II. The constraints are quite severe for fitting spectral shapes and angular distributions simultaneously, and hence we can assign relatively small uncertainties to the derived (model-dependent) parameters (see footnotes to Table II). Systematically, the spherical alpha-evaporation barriers which reproduce the data are significantly low, as has been suggested previously [6,17,19,21–23,50–60], but the proton-evaporation barriers require even more drastic decreases to match the experimental energy spectra [51,61,62].

Let us reconsider (see Sec. III A) the contributions to the observed inclusive particle spectra resulting from ^{1}H/^{4}He evaporation from reaction fragments (e.g., fission, projectile-like). Clearly, such contributions would be most prominent for the heavier systems studied. As indicated earlier, for reaction 10 (^{121}Sb$+^{27}$Al) we have made extensive coincidence measurements involving fragments and particles as well as particle-particle correlations [44]. The fragment-particle data demonstrate that the inclusive ^{1}H/^{4}He energy spectra are dominated by emissions from evaporation residues. Furthermore, fragment-particle-particle triple coincidences indicate that the particle-particle coincidences arise mainly from the evaporation residues [23,44], and hence provide a filter for selecting out such emissions (or of eliminating fragment-associated emissions). We show in Fig. 7 a comparison of representative ^{1}H and ^{4}He inclusive spectra with the corresponding spectra gated by a coincident ^{4}He particle. Although these data are from reaction 10, we expect the other heavy systems to behave similarly. At each angle shown, we have normalized the inclusive measurements to the coincidence data and indicated the normalization factors (N). The slow variation of the normalization factor with angle results from slightly different angular distributions for the two data sets. The important point is that the coincidence spectra have nearly identical shapes with the inclusive spectra over the angular range shown, and the differences between the two occur primarily in spectral energy regions which are of little consequence in fitting the data. The solid curves in Fig. 7 were obtained from statistical model calculations using GANES to simulate the expected ^{1}H and ^{4}He spectra in coincidence with a ^{4}He trigger particle. These calculations employed the same basic parameter set which was extracted from fitting the inclusive energy spectra and angular distributions for this reaction, as indicated in Table II. The excellent agreement between these fits for the particle-particle coincidence data and the inclusive data strongly implies that fragment emission is not a serious problem here and gives confidence in the results summarized in Table II.

To what, then, can we attribute the observed systematic discrepancies between the experimental ^{1}H and ^{4}He data and the predictions from the standard statistical model calculations for spherical nuclei? This question is addressed in Secs. III D and III E, where we consider some of the approximations made in carrying out the statistical model calculations and the appropriateness of the model itself. First, however, we present in the next section some additional experimental data which must also be understood in the context of an adequate evaporation model.

C. Relationships among evaporative protons, deuterons, and tritons

In addition to protons and alpha particles, other light charged particles are often evaporated from hot composite nuclei in substantially lower yield. For several of the experiments reported here, deuterons and tritons were measured with sufficient statistical accuracy to provide reliable energy spectra. We display in Fig. 8 a comparison of representative proton, deuteron, and triton spectra for two of the reactions studied, 167-MeV ^{20}Ne$+^{27}$Al and 190-MeV ^{40}Ar$+^{27}$Al. Qualitatively, the data for ^{2}H and ^{3}H appear very similar to the corresponding ^{1}H data in Fig. 8, exhibiting the characteristic features associated with evaporation from thermally equilibrated nuclear systems. The solid curves in Fig. 8 were calculated with the statistical model code GANES using the constrained parameter sets given for each reaction in Table II. In particular, the fusion cross sections [46] in the entrance channel were used to limit the maximum angular momenta, J_{crit}, in the composite systems, and the exit-channel evaporation barriers for protons were derived from fusion barrier systematics [47] for the corresponding inverse reactions. The barriers for ^{2}H and ^{3}H were taken as equal to that for ^{1}H in the same system. As demonstrated earlier in Fig. 5, this prescription predicts ^{1}H spectra which are significantly higher in energy than the ^{1}H data. We can see this shift again for the ^{1}H results in Fig. 8. However, the statistical model calculations for ^{2}H and ^{3}H bear a much closer relationship to the data for each of the two reactions. There is only a small shift between the measured and calculated ^{2}H spectra, and for ^{3}H there is excellent agreement of the predictions with the data. Such results are indeed surprising, as has been noted recently for heavier systems [23,52]. The behavior summarized in Fig. 8 could contain an important clue to the discrepancies between measured ^{1}H and ^{4}He evaporation barriers and their predicted counterparts based upon constrained statistical model calculations. Certainly, whatever explanations are put forth must encompass the full complement of observations, including ^{2}H and ^{3}H data as well as ^{1}H and ^{4}He.

D. The roles of multistep particle emission and competition in the model calculations

In the present study we have used the statistical model code GANES [45] to calculate the expected properties of evaporative ^{1}H/^{4}He under the assumption of statistical equilibrium. This code offers considerable versatility in the selection and modification of the constraining equilibrium parameters, and allows the calculation of energy spectra for particles correlated with specific characteristics of heavy reaction fragments or other light charged particles. Because it employs the weighted Monte Carlo technique, it is able to provide good statistical precision with only modest demands on computer time. The code does, however, treat the evaporation process as an equivalent one- (or two-) step particle emission, rather than following the entire evaporation cascade over many steps. Thus the user must specify the properties (Z, A, E^*, and J) to be associated with the average emitter. This approximation should be valid if the particle emission probability is roughly constant along the evaporation chain, but could lead to inaccuracies if the particular type of particle were preferentially emitted late in the cascade.

It is worthwhile exploring the differences which result from equivalent one-step versus multistep particle emission in the statistical evaporation calculations. To do this we have performed a series of tests using a Monte Carlo code LILITA_N90 [63,64], which models statistical evaporation by following the particle emission from a compound nucleus through each step of the entire cascade. Both the multistep and equivalent one-step calculations were carried out using the same code. Our test results are summarized in Fig. 9. In this figure we show several sets of calculated spectra, ^{4}He on the left and ^{1}H on the right, for two of the reactions in Table I. We specifically selected light systems for the present tests, because differences between multistep and one-step calculations are likely to be greater than for heavy systems. In each case, the points represent multistep LILITA_N90 calculations and the solid curve corresponds to the equivalent one-step LILITA_N90 result. As the curves are quite close to the corresponding sets of points for both ^{4}He and ^{1}H emissions, we believe that Fig. 9 demonstrates that the equivalent one-step approximation is valid for these systems. For comparison, the experimental spectra are given in Fig. 9 as histograms. It is clear that the differences between experiment and calculations are much larger than any deviations between the equivalent one-step and multistep calculations.

In a recent study, La Rana *et al.* [54,65] have made comparisons between LILITA [64] and GANES for the reaction 120-MeV ^{30}Si+^{30}Si. They verified that the two codes yielded nearly identical ^{4}He spectra when both codes were run for first-step emission, and the values of the relevant physical parameters (barriers, radius parameters, level density parameters, etc.) were made the same. Furthermore, they have compared LILITA multistep calculations with equivalent one-step calculations, also performed with LILITA, and have shown the ^{4}He energy spectra to be very similar for their system.

Thus it appears that the use (in the code GANES) of an average emitter in lieu of the summation over successive emissions does not lead to spectral energy shifts of the magnitude required to explain the discrepancies illustrated in Figs. 5 and 6. This is not surprising when one realizes (as will be shown in Sec. III F) that the shift in effective emission barrier of a compound nucleus is only about 0.1 MeV per Z unit for ^{1}H evaporation and about 0.22 MeV per Z for ^{4}He evaporation. Hence even long chains of particle emissions should be reasonably represented by an average effective emission, provided the near-yrast emission is not extreme. Yrast-line effects exert a greater influence on ^{4}He emission, compared to

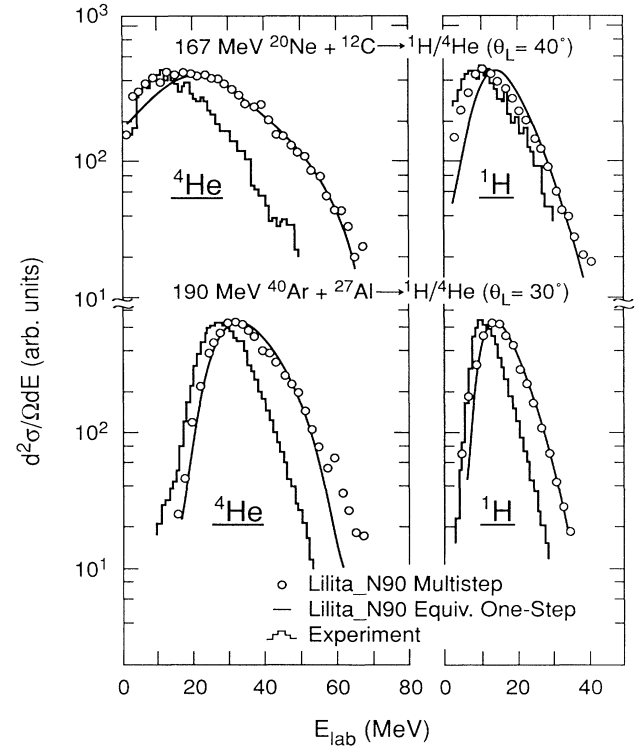

FIG. 9. Comparisons of statistical model calculations of ^{4}He spectra (left) and ^{1}H spectra (right) for ^{20}Ne+^{12}C reactions (top) and ^{40}Ar+^{27}Al reactions (bottom). The points come from a multistep evaporation calculation, including particle competition, using the code LILITA_N90 [63,64]. The solid curves result from an equivalent one-step calculation (without competition) using the same LILITA_N90 code. The experimental energy spectra are shown as histograms.

^{1}H evaporation, because of the presence in the multistep codes of enhanced near-yrast alpha-particle emission [66]. The detailed treatment of gamma-ray competition and near-yrast emission will certainly modify the particle emission near the end of the evaporation chain, and therefore can affect the overall emission pattern. However, in the present context our sole purpose in using the LILITA_N90 code is to demonstrate that the apparent barrier shifts required by the experimental data are not an artifact of using an equivalent-one-step code. Therefore, for the comparison tests whose results are shown in Fig. 9, the gamma-ray competition had been turned off and the particle emission was terminated when the transmission coefficients were less than 10^{-3}.

In a related manner, the recent report of Govil *et al.* [67] shows a decrease in the average calculated ^{4}He energy which results from suppression of early step ^{4}He emission by the use of a spin-dependent moment of inertia. These authors do not comment on the corresponding ^{1}H emission energies. Since ^{1}H, ^{2}H, or ^{3}H emissions are not particularly favored by proximity to the yrast line, energy shifts arising from this source are not anticipated for these particles. Hence the apparent low barriers required for matching the ^{4}He and ^{1}H data (see Figs. 5, 6, and 8) cannot be attributed solely to yrast effects or to competition along the evaporation chain. The fact that the observed shifts in the ^{1}H spectra are even larger than those for ^{4}He strongly suggests that one must seek a common, or related, origin to explain the effects observed for both particles.

E. The effects of nuclear deformation

We have seen from the results presented in Figs. 5 and 6 and Table II that the statistical model calculations require substantial reductions in emitter barriers and spins in order to fit the experimental ^{1}H/^{4}He data. This systematic behavior, observed for all the reactions in Table I, demonstrates over a broad Z range that evaporation from excited compound nuclei is substantially different from the inverse process of fusion between cold ground-state nuclei. A natural expectation is that these differences arise from deformation of the hot, high-spin, composite systems. The qualitative effects of such deformations would be to dampen the spin contributions by enlarged moments of inertia [see Eq. (1)], and emission barriers would be lowered in regions of large radial extent. Therefore it is worthwhile to estimate quantitatively the influence of these effects on the experimental observables.

To carry out such a test of nuclear deformation, we have attempted to fit the measured particle spectra with statistical model evaporation calculations that explicitly treat the deformation in a self-consistent manner. A Cassini shape representation has been used within the framework of the GANES code, as described in detail in Ref. [49]. Briefly, the nuclear shape is characterized by a single parameter $\tilde{\varepsilon}$, whose value determines both the moments of inertia and the nuclear charge distribution at each point of the nuclear surface. (The value $\tilde{\varepsilon}=0$ yields a spherical nucleus, and $\tilde{\varepsilon}=1$ corresponds to two equal-mass nuclei touching at a single point.) Thus the effective emission barriers and the yrast line (or moments of inertia) are derived simultaneously and consistently. In these calculations, the values of J were fixed to $J_{\text{rms}}=(J^2_{\text{crit}}/2)^{1/2}$ from fusion cross-section data, and the particle emission barriers were calculated from the Coulomb-nuclear potential (of the deformed nucleus) using a 50-point grid around the nuclear surface. The nuclear potential was of a Woods-Saxon form whose diffuseness was adjusted to reproduce empirical fusion barriers between cold (spherical) nuclei. The calculations were carried out systematically allowing only two quantities to vary, the nuclear shape $\tilde{\varepsilon}$, and the mean excitation energy E^*, until the best fit to the data was obtained.

The results from the deformed-nucleus calculations are presented in Figs. 10 and 11. The experimental data are the same as in Figs. 5 and 6, respectively, and the solid curves here represent the fits achieved with the deformed-nucleus model. As before, the ^{4}He spectra are on the left and the ^{1}H spectra are on the right for each reaction indicated. The ^{4}He calculations are able to reproduce the experimental data reasonably well, the quality of the fits being comparable to, but not quite as good as, the unconstrained fits in Figs. 5 and 6 (solid curves). (Generally, the ^{4}He energy spectra calculated with the deformed model fall off somewhat more steeply on the low-energy sides of the spectra, compared to the calculations from the unconstrained spherical model.) However, the overall agreement between calculation and experiment for the ^{4}He spectra in Figs. 10 and 11 suggests that nuclear deformation may be important in the evaporative deexcitation of the hot composite nuclei.

From the ^{4}He fits in Figs. 10 and 11, we have derived the effective excitation energies and shape parameters yielded by the deformed nuclear model. These are listed in Table III for each of the ten reactions. The first column gives the reacting system, followed in column 2 by the excitation energy required to fit the ^{4}He spectrum. These energies are all substantially lower than the initial excitation energies for the same reasons discussed in Sec. III B, and are rather similar to the effective excitation energies derived from the fits with the unconstrained spherical model (see column 7 in Table II). Column 3 shows the root-mean-square values of the entrance-channel spin distributions, corresponding to the values of J_{crit} derived from fusion cross sections and listed in Table II. As indicated above, these spin values were not allowed to vary in the deformed model calculations. Column 4 gives the Cassini deformation parameter [68] $\tilde{\varepsilon}$ which best fits the data, and column 5 is the ratio of major-to-minor axes for the near-prolate shapes resulting from the specified values of $\tilde{\varepsilon}$. Examination of this last column leads to the striking conclusion that very large deformations are required to account for the observed ^{4}He spectra. Large deformations have been inferred before from several studies of particle evaporation prior to fission [10,22,53,69–72]. But for the nuclear systems in Table III, most of which do not undergo fission, it seems unlikely that evaporation would occur from forms stretched even beyond the equilibrium saddle-point shapes [73–75]. It is interesting to note that recent neutron emission studies [76] also suggest evaporation from configurations which appear to be very highly stretched.

Let us now examine the ^{1}H data in Figs. 10 and 11. Here the deformed model calculations were carried out using the same parameter sets (shape $\tilde{\varepsilon}$, excitation E^*, and spin J_{rms}) which produced the good fits for the corresponding ^{4}He spectra. However, the calculated ^{1}H spectra (solid curves) fall far short of representing the experimental spectra, being always shifted to higher energies than the data. In fact, the observed ^{1}H spectra have such low energies (and effective spherical barriers—see Table II) that it is impossible to fit them with any reasonable shape within the framework of our deformed-nucleus model. It is quite clear from the comparisons in Figs. 10 and 11 that while (unreasonably) large deformations could be responsible for the observed low energies of the

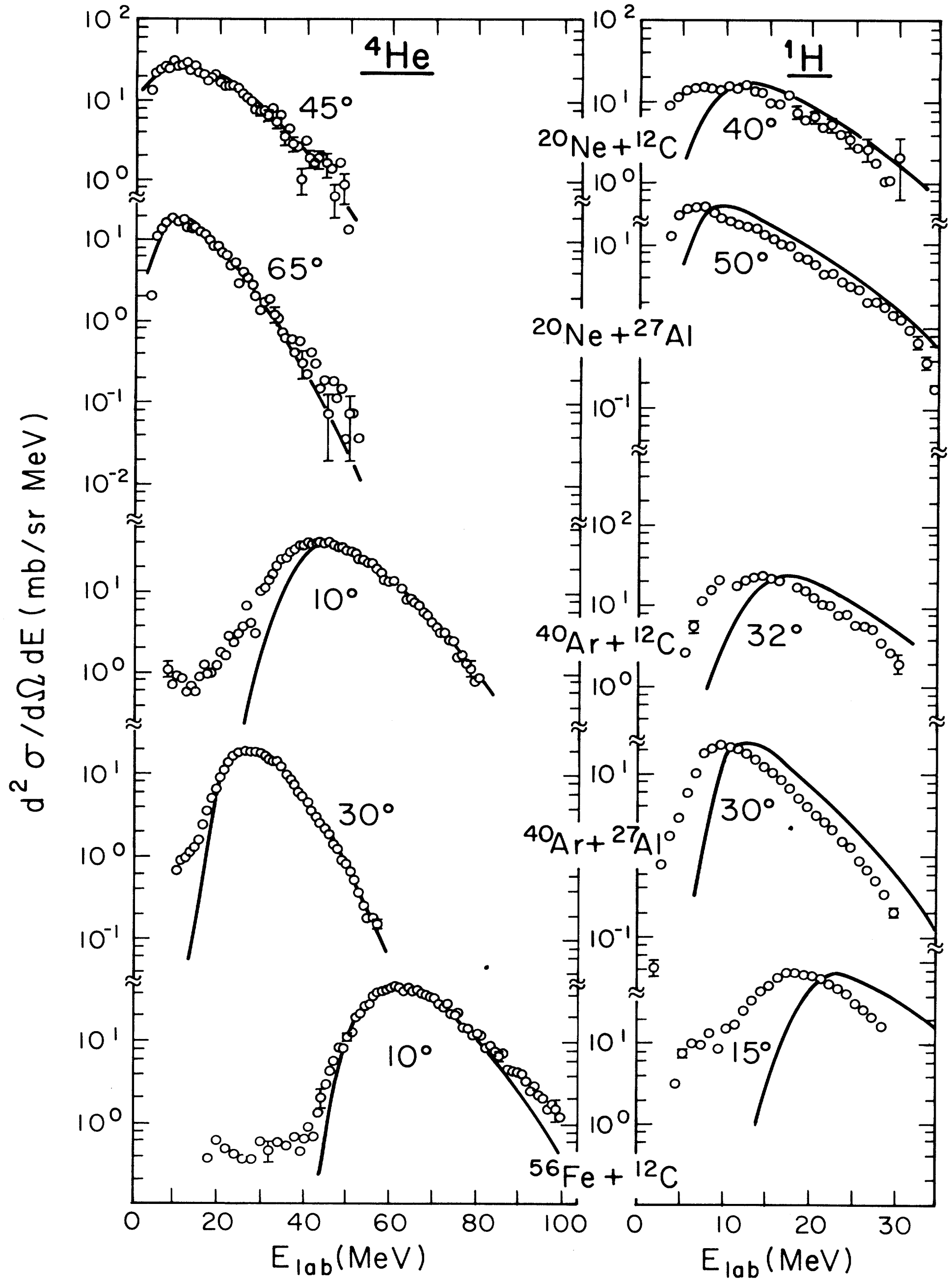

FIG. 10. Comparison of experimental ^{4}He/^{1}H energy spectra for reactions 1–5 (see Table I) with statistical model calculations for deformed nuclei (solid curves). The data (points) are the same as in Fig. 5, and the calculations employed the parameters given in Table III.

^{4}He spectra, there is no way that nuclear deformation alone can account for the measured very low ^{1}H energies. The remaining differences are substantial over the whole Z range represented by the systems in Figs. 10 and 11.

What can we infer from these discrepancies? It seems quite likely that a major physical effect has yet to be included in the evaporation model. Nuclear deformation seems to be insufficient to adequately explain the low emission barriers. There must be some other property of the transition states that gives an increase in the radial distance between the emerging charged particles and the residual nucleus. Normal thermal expansion of a Fermi gas has been studied theoretically [77,78], and this effect is already included in our Monte Carlo calculations. Furthermore, we must account for the observed trends in effective emission barriers for ^{1}H, ^{2}H, and ^{3}H (see Sec. III C and Fig. 8).

We speculate [23,51–53] that the surface density

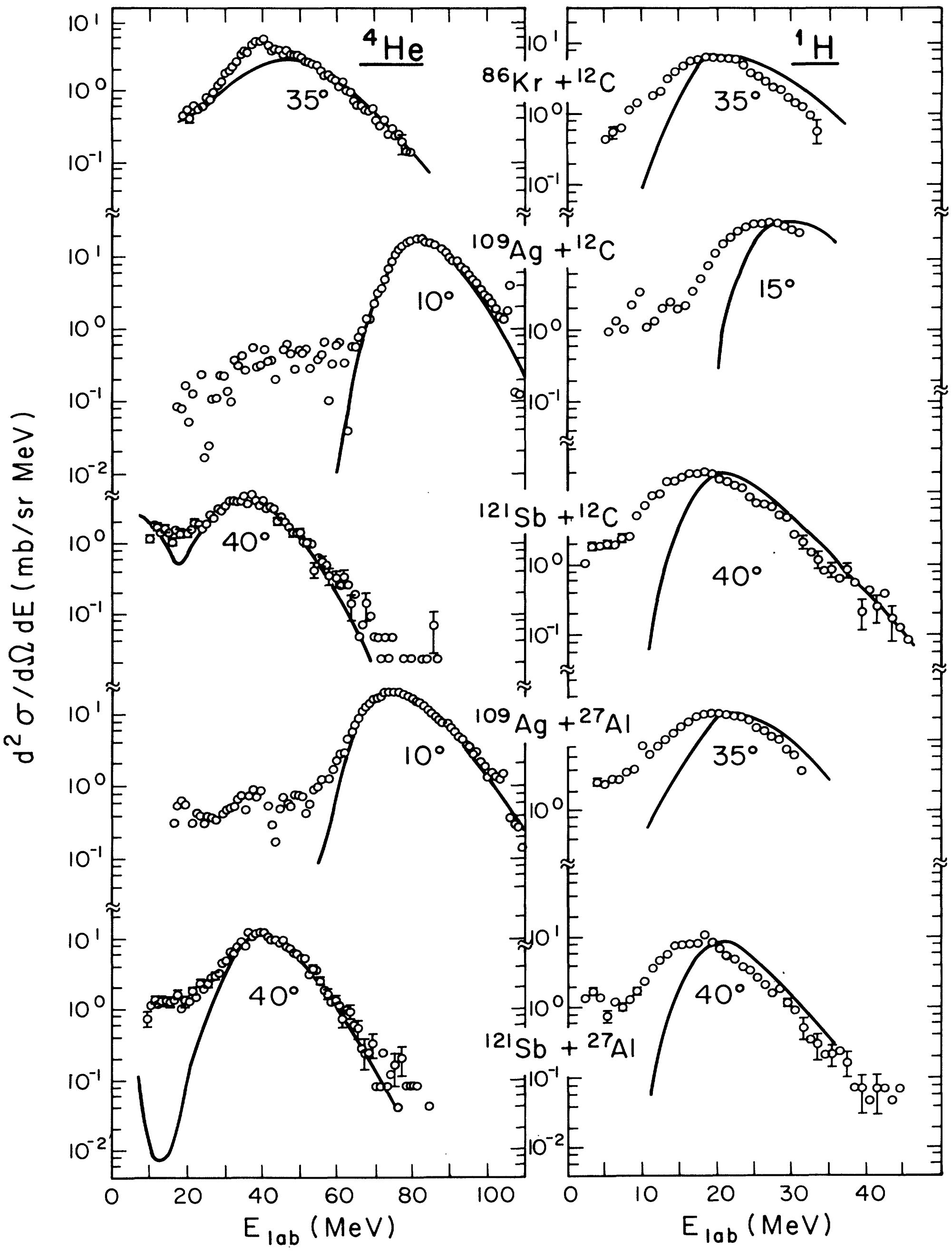

FIG. 11. Same as Fig. 10, but for the reactions 6–10 in Table I. The data (points) are the same as in Fig. 6.

profiles of the hot nuclei have much longer tails than usually expected. Furthermore, this phenomenon is indicated over the broad range of hot nuclear systems considered here. Perhaps in the early stages of reaction the collision excites primarily those nucleons near the surface of the nucleus. The Pauli principle would tend to favor the excitations in these outer orbitals. Hence the transient nuclear matter distribution may be far from uniform, and evaporation-like particle emission may occur before complete relaxation of the nuclear density. In the outer fringes of the reacting system, the emission barriers would be lower than in the central region, resulting in unexpectedly low average particle energies, as we observe for protons. If we consider the probability for cluster formation to be a strong function of the nucleonic density, then we can infer that ^{2}H and ^{3}H are preferentially emitted from regions of higher density, and hence more normal emission energies are encountered. For ^{4}He, the exceptionally high binding energy may lead to an intermediate situation, where the preformation is enhanced enough to allow emission from lower density regions, but not as remote from the nuclear interior as projected for proton emission.

Is it reasonable to propose such extreme variations in the nuclear surface? Recent theoretical studies [79] suggest there may be a physical basis for the idea. Hartree-Fock calculations [80,81] show that self-consistent nuclear density distributions for hot nuclei evolve into a contracted volume region and into an elongated surface tail, the latter corresponding to the formation of a nuclear stratosphere by the occupation of high-lying single-particle orbits.

The scenario just described involves dynamical features not ordinarily included in models of statistical evaporation. We refer to these as "dynamical" because they are not phase-space related and evolve as the reaction proceeds. As qualitatively proposed, these new features can offer a way of understanding why proton evaporation exhibits large apparent barrier reductions, while this tendency is much less for deuterons and virtually absent for tritons (see Fig. 8). If the intermediate behavior of ^{4}He is a consequence of its special binding energy, then one might expect clusters like Li, Be, and B to exhibit evaporation barriers which are not significantly lowered relative to the corresponding (inverse) fusion barriers. It will be of considerable interest to make such comparisons in the future, as the appropriate experimental data become available [29,82–85].

F. Empirical systematics of charged-particle evaporation barriers

We have demonstrated, above, that widespread discrepancies exist between experimental evaporative ^{1}H/^{4}He energies and the predictions of statistical model

TABLE III. Calculated results for ^{4}He evaporation from deformed emitters. Parameters derived by fitting the experimental ^{4}He energy spectra and angular distributions with an evaporation model for deformed nuclei. In these calculations, the effective spins of the emitters were derived from cross-section data [46] and were not free parameters. For the corresponding proton data, adequate fits were not obtained with the deformation model (see Figs. 10 and 11).

System	E^{*a} (MeV)	$J_{\text{rms}}{}^{b}$ ($\hbar$)	$\bar{\varepsilon}^{c}$	$(d_1/d_2)^{d}$
167-MeV ^{20}Ne+^{12}C	48.6	16	0.70	2.4
167-MeV ^{20}Ne+^{27}Al	79.8	21	0.70	2.4
340-MeV ^{40}Ar+^{12}C	59.4	25	0.72	2.5^{e}
190-MeV ^{40}Ar+^{27}Al	63.7	32	0.70	2.4
476-MeV ^{56}Fe+^{12}C	54.6	28	0.70	2.4^{e}
730-MeV ^{86}Kr+^{12}C	87.4	34	0.10	1.1^{e}
956-MeV ^{109}Ag+^{12}C	64.4	28	0.50	1.7
1030-MeV ^{121}Sb+^{12}C	53.4	28	0.60	2.0
956-MeV ^{109}Ag+^{27}Al	106.0	47	0.70	2.4
1030-MeV ^{121}Sb+^{27}Al	94.2	46	0.80	3.0

[a] Effective excitation energy of the emitter. The uncertainty in E^* is ±10%.

[b] Root-mean-square spin of the composite system, obtained from $J_{\text{rms}} = (J^2_{\text{crit}}/2)^{1/2}$.

[c] Cassini deformation parameter [68] $\bar{\varepsilon}$, derived from fitting the experimental data with the deformed-nucleus model. The uncertainty in $\bar{\varepsilon}$ is approximately ±0.05. For orientation, $\bar{\varepsilon}=0$ is a sphere and $\bar{\varepsilon}=1.0$ corresponds to two elongated objects toucning at a single point at the center of symmetry (Bernoulli lemniscate).

[d] Ratio of major-to-minor axes of the deformed emitter. These values are derived from the corresponding $\bar{\varepsilon}$ value in column 4. An uncertainty of ±0.05 in $\bar{\varepsilon}$ yields an uncertainty of approximately 0.2–0.3 in the ratio (d_1/d_2).

[e] Calculations for these three systems have been reported earlier [35]. The parameters given here (and in Table II) differ slightly from the previous values due to small changes in the computer code and improvements in the fitting procedure. The earlier axis ratios [35] involved an error which has now been corrected.

calculations for spherical nuclei, using *a priori* parameters (i.e., emission barriers derived from fusion barriers and spins derived from cross-section data). We have also shown that nuclear deformation could possibly play a significant role, but by itself cannot explain the range of experimental observables in a reasonable way. In particular, the proton energies are much too low to be accounted for by deformation, the deuteron and triton energies are much less shifted, compared to spherical model expectations, and the ^{4}He energies, if explainable by deformation, would require nuclear elongations which are unreasonably large (see Table III) for hot composite nuclei that survive fission. Although we have suggested a dynamical mechanism which, when superimposed on statistical evaporation, might account for the observed charged-particle characteristics, our current knowledge of the transient states of nuclear matter is too immature to offer much confidence in quantitative detail. Rather, we must continue the search for new experiments and theoretical models which will provide critical tests and/or predictions, in order to build a secure framework for understanding the behavior of highly excited complex nuclei.

On the other hand, our results in Figs. 5 and 6 (solid curves), and Table II (last three columns), indicate that excellent fits to both the experimental ^{1}H and ^{4}He spectra can be obtained by employing effective evaporation barriers (and spins) which are systematically lowered from the *a priori* values. The development of such empirical barrier systematics, over a broad range of hot composite nuclei, can serve several useful purposes without detracting from the long-range goal of understanding the origins of the lowered barriers. For example, the study of empirical charged-particle evaporation barriers can help to elucidate the properties of highly excited nuclei, in distinction to the corresponding properties already known for their cold ground-state counterparts. This idea has been emphasized earlier in the work of Alexander *et al.* [50], who considered the available ^{4}He evaporation data for a number of systems and parametrized the effective *s*-wave barriers in terms of the average channel energies derived from the spectra. Similarly, empirical prescriptions which relate the *s*-wave emissions barriers for ^{4}He and ^{1}H to the observed properties of the emitters as a function of Z and A can assist in the calibration of evaporation calculations based upon statistical theory. This latter application is of importance in many practical situations, where the objective is to quantitatively fit experimental spectra with model calculations in order to extract particle multiplicities or to discriminate one reaction mechanism from another.

As described in Sec. III B, we have used the Monte Carlo code GANES [45] to calculate the ^{1}H/^{4}He evaporation spectra at the relevant angles for comparison with the experimental data. The empirical fits obtained for ^{1}H and ^{4}He emission from the ten reactions studied here have been represented by the solid curves in Figs. 5 and 6, and the extracted "best-fit" parameters have been tabulated in the last three columns of Table II. These empirical results are more firmly grounded, compared to the earlier approach [50], since the full shapes of the evaporation spectra have been considered, rather than the average energies, and the data have been compared in a self-consistent manner with the spectra calculated from statistical evaporation theory. In addition, the systematics of ^{1}H evaporation barriers are presented here for the first time [86].

The empirical barrier systematics derived from our work are summarized in Fig. 12, where we have plotted the *s*-wave evaporation barrier, B, as a function of emitter Z. The upper half of Fig. 12 gives ^{1}H results, and the lower half is for ^{4}He. The data plotted as circles are the spherical-fit barriers from column 9 in Table II, vs the effective atomic number in column 6. We have also included the squares from Ref. [23] and the triangles from Ref. [53], as these results were obtained using the same procedures as in the present study. The solid curves in each half of the figure result from attempts to describe the empirical evaporation barriers over the full Z range by smooth analytical functions. For the ^{4}He data, the function used retains the form of a simple Coulomb po-

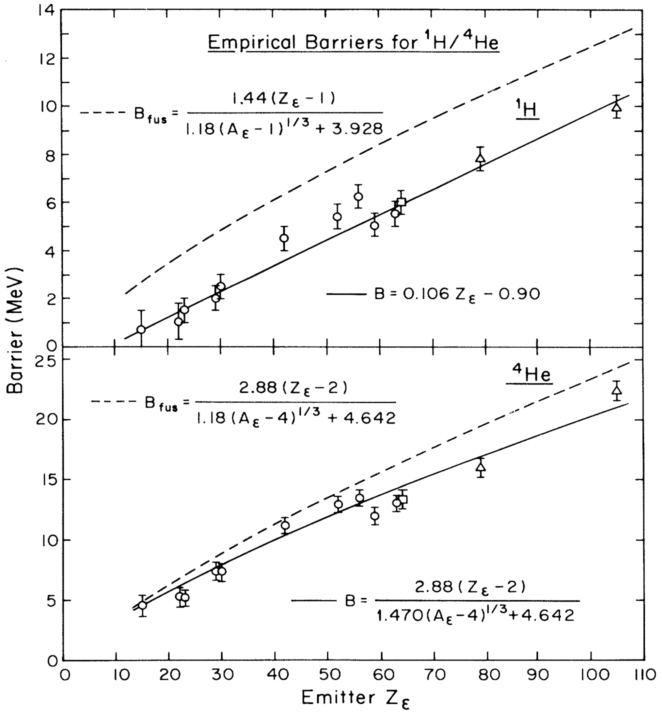

FIG. 12. Empirical evaporation barriers for ^{1}H (top) and ^{4}He (bottom). The circles are the fitted *s*-wave barriers from the spherical nucleus model (see Table II). The squares are from Ref. [23] and the triangles are from Ref. [53]. The solid lines are prescriptions which represent the empirical barriers as a function of the emitter atomic number, Z_ε. For comparison, the dashed lines give the corresponding fusion barriers from reaction systematics [47]. The analytical representations of the solid and dashed lines are indicated.

tential, and is given by the equation

$$B(^4\mathrm{He})=\frac{2.88(Z_\varepsilon-2)}{1.470(A_\varepsilon-4)^{1/3}+4.642}\ , \tag{3}$$

where Z_ε and A_ε are the effective atomic and mass numbers of the average emitting system. The ^{1}H results are adequately described by a linear relation, which we have given as

$$B(^1H)=0.106Z_\varepsilon-0.90\ , \tag{4}$$

over the Z range 15–105. For comparison, the dashed curves in Fig. 12 represent functional descriptions of the systematics [47] for fusion barriers, B_{fus}, derived from experimental ^{1}H and ^{4}He reaction cross-section data. As can be easily seen, the empirical ^{4}He evaporation barriers fall systematically below the corresponding fusion barriers, as has already been noted in the previous discussion in Sec. III B. The ^{1}H evaporation barriers are clearly much lower (~2 MeV) than the fusion barriers over the full Z range investigated. Two additional comments should be made concerning the solid lines in Fig. 12, and the corresponding Eqs. (3) and (4). First, Eqs. (3) and (4) have no significance beyond their representation of the empirical barriers, and there may be other relationships which would serve as well. In other words, no theoretical basis is necessarily implied for their origin. Second, in arriving at the values of the numerical constants in these equations, we considered a larger data set than shown in Fig. 12. Our stated purpose in the present paper is to analyze and interpret only our own experimental measurements, to avoid the greater uncertainties and possible ambiguities associated with treating data from diverse origins. In a future paper [36], we plan to discuss the systematics of empirical evaporation barriers using the results of the larger data set obtained from the published literature. In anticipation of that work, we have selected the constants in Eqs. (3) and (4) using all of the data, not just our own experimental results. However, this formulation does a respectable job in describing the data in Fig. 12, as well.

It is clear that the systematics of evaporation barriers represented by Eqs. (3) and (4) and Fig. 12 are an oversimplification in that only the composition of the nuclear emitters is explicitly considered. We have already indicated (see Table II and Sec. III B) that the effective spins (or moments of inertia) must be modified, particularly for the lighter nuclei, in addition to the Coulomb barriers, in order to fit the experimental data using a spherical nucleus model. Similarly, there is growing experimental evidence [6,19,87–94] that the effective level densities of excited nuclei may depend on entrance-channel spin, presumably as a consequence of possible changes in nuclear shape (hence moments of inertia) with spin. In effect, Eqs. (3) and (4) (and Fig. 12) implicitly average over spin for the emitters considered, and this approximation may account in part for individual deviations from the smooth trends.

We are currently using Eqs. (3) and (4) as default empirical evaporation barriers in the code GANES8, in the option invoking a spherical nuclear model to fit experimental ^{1}H/^{4}He energy spectra or predict the shapes of such spectra for unmeasured or unknown emitters.

IV. SUMMARY AND CONCLUSIONS

We have studied ten reactions (nine in reversed kinematics) leading to composite nuclei over the broad Z range from 16 to 64. Light charged-particle spectra and angular distributions were measured under conditions of low effective energy thresholds, permitting detailed comparisons with statistical model predictions. By means of invariant cross-section maps and coincidence measurements for typical systems, we have been able to focus for each reaction on specific angular regions where the dominant source of evaporative charged-particle emission is the composite system. Statistical model calculations for spherical nuclei yield particle energies which are substantially higher than observed, when the calculations are carried out using emission barriers from fusion systematics, spin distributions from cross-section data, and spherical moments of inertia. Comparisons of proton, deuteron, and triton spectra for several of the reactions reveal significant trends which also are not reproduced by the model calculations. Using the multistep evaporation code LILITA__N90, we show that the discrepancies between the experimental spectra and theory do not result from the equivalent one-step approximation employed in the code GANES. Rather, the imposed constraints on barriers, spins, and moments of inertia lead to the observed spectral shifts. Statistical model calculations of evaporation from deformed nuclear emitters suggest that large deformations may be present, but in addition, other effects not included in the model must play an important role. This is because the deformed model calculations (with very large nuclear elongations) can adequately reproduce the ^{4}He energy spectra, but are unable to predict the corresponding very low proton energies which are observed. We propose a dynamical transition-state model in which energy sharing among the various degrees of freedom has been achieved, but in which the nuclear matter density distribution has not yet attained its ground-state properties. This implies a long tail in the radial distribution of nucleonic matter, the existence of which seems to be supported by recent theoretical studies. Such a model, together with the additional requirements of preformation for nucleonic clusters, can at least qualitatively explain the observed low emission barriers for ^{1}H/^{4}He and the energetic trends found for ^{1}H/^{2}H/^{3}H evaporation.

By removing the emission barrier and spin constraints in the model calculations, we obtain excellent fits to all of the experimental spectra and angular distributions using systematically lowered barriers and spin distributions within a spherical model framework. This provides the basis for developing empirical systematics of charged-particle evaporation barriers, and we present results for the ten systems studied here. Simple analytical expressions are given which represent the empirical barriers for ^{1}H and ^{4}He, and these may be useful in other applications involving model calculations.

ACKNOWLEDGMENTS

We wish to thank the staff of the Lawrence Berkeley Laboratory SuperHILAC for the excellent support provided in the course of many experiments. Particular appreciation is due to Bill Rathbun for assistance with the data-acquisition system, and for his extra efforts in keeping our experiments on track. This work was supported by the Division of Nuclear Physics, Office of High Energy and Nuclear Physics, U.S. Department of Energy.

---

*Present address: Los Alamos National Laboratory, Los Alamos, NM 87545.

†Permanent address: Instituto Nazionale di Fisica Nucleare, Mostra d'Oltremare, Pad. 20, Naples 80125, Italy.

‡Permanent address: International Business Machines Corporation, Kingston, NY 12401.

§Present address: National Superconducting Cyclotron Laboratory, Michigan State University, East Lansing, MI 48824.

**Permanent address: Department of Physics, Hope College, Holland, MI 49432.

[1] M. Kildir, D. Logan, M. Kaplan, M. S. Zisman, D. Guerreau, J. M. Alexander, and L. C. Vaz, Z. Phys. A **306**, 323 (1982).

[2] M. Rajagopolan, D. Logan, J. W. Ball, M. Kaplan, H. Delagrange, M. F. Rivet, J. M. Alexander, L. C. Vaz, and M. S. Zisman, Phys. Rev. C **25**, 2417 (1982).

[3] M. F. Rivet, D. Logan, J. M. Alexander, D. Guerreau, E. Duek, M. S. Zisman, and M. Kaplan, Phys. Rev. C **25**, 2430 (1982).

[4] N. N. Ajitanand, J. M. Alexander, H. Delagrange, E. Duek, D. O. Eriksen, D. Guerreau, M. Kaplan, M. Kildir, L. Kowalski, R. Lacey, D. Logan, D. J. Moses, G. F. Peaslee, L. C. Vaz, and M. S. Zisman, Z. Phys. A **316**, 169 (1984).

[5] C. Borcea, E. Gierlik, R. Kalpakchieva, N. H. Chau, Y. T. Oganessian, T. Pawlat, and Y. E. Penionzhkevich, Nucl. Phys. **A415**, 169 (1984).

[6] R. K. Choudhury, P. L. Gonthier, K. Hagel, M. N. Namboodiri, J. B. Natowitz, L. Adler, S. Simon, S. Kniffen, and G. Berkowitz, Phys. Lett. **143B**, 74 (1984).

[7] H. Delagrange, A. Benachou, F. Hubert, Y. Llabador, B. Heusch, J. P. Coffin, P. Engelstein, P. Fintz, and G. Guillaume, Nucl. Phys. **A429**, 173 (1984).

[8] T. Fukuda, M. Ishihara, H. Ogata, I. Miura, T. Shimoda, K. Katori, S. Shimoura, M. K. Tanaka, E. Takada, and T. Otsuka, Nucl. Phys. **A425**, 548 (1984).

[9] L. G. Sobotka, M. A. McMahan, R. J. McDonald, C. Signarbieux, G. J. Wozniak, M. L. Padgett, J. H. Gu, Z. H. Liu, Z. Q. Yao, and L. G. Moretto, Phys. Rev. Lett. **53**, 2004 (1984).

[10] L. C. Vaz, D. Logan, E. Duek, J. M. Alexander, M. F. Rivet, M. S. Zisman, M. Kaplan, and J. W. Ball, Z. Phys. A **315**, 169 (1984).

[11] D. Jacquet, J. Galin, B. Borderie, D. Gardes, D. Guerreau, M. Lefort, F. Monnet, M. F. Rivet, X. Tarrago, E. Duek, and J. M. Alexander, Phys. Rev. C **32**, 1594 (1985).

[12] K. T. Lesko, W. Henning, K. E. Rehm, G. Rosner, J. P. Schiffer, G. S. F. Stephans, B. Zeidman, and W. S. Freeman, Phys. Rev. Lett. **55**, 803 (1985).

[13] E. Bozek, D. M. de Castro Rizzo, S. Cavallaro, B. Delaunay, J. Delaunay, H. Dumont, A. D'Onofrio, M.-G. Saint-Laurent, L. Sperduto, and F. Terrasi, Nucl. Phys. **A451**, 171 (1986).

[14] R. J. Charity, M. A. McMahan, D. R. Bowman, Z. H. Liu, R. J. McDonald, G. J. Wozniak, L. G. Moretto, S. Bradley, W. L. Kehoe, A. C. Mignerey, and M. N. Namboodiri, Phys. Rev. Lett. **56**, 1354 (1986).

[15] A. Gavron, A. Gayer, J. Boissevain, H. C. Britt, J. R. Nix, A. J. Sierk, P. Grange, S. Hassani, H. A. Weidenmuller, J. R. Beene, B. Cheynis, D. Drain, R. L. Ferguson, F. E. Obenshain, F. Plasil, G. R. Young, G. A. Petitt, and C. Butler, Phys. Lett. B **176**, 312 (1986).

[16] D. J. Hinde, R. J. Charity, G. S. Foote, J. R. Leigh, J. O. Newton, S. Ogaza, and A. Chatterjee, Nucl. Phys. **A452**, 550 (1986).

[17] G. Nebbia, K. Hagel, D. Fabris, Z. Majka, J. B. Natowitz, R. P. Schmitt, B. Sterling, G. Mouchaty, G. Berkowitz, K. Strozewski, G. Viesti, P. L. Gonthier, B. Wilkins, M. N. Namboodiri, and H. Ho, Phys. Lett. B **176**, 20 (1986).

[18] A. Gavron, A. Gayer, J. Boissevain, H. C. Britt, T. C. Awes, J. R. Beene, B. Cheynis, D. Drain, R.L. Ferguson, F. E. Obenshain, F. Plasil, G. R. Young, G. A. Petitt, and C. Butler, Phys. Rev. C **35**, 579 (1987).

[19] Z. Majka, M. E. Brandan, D. Fabris, K. Hagel, A. Menchaca-Rocha, J. B. Natowitz, G. Nebbia, G. Prete, B. Sterling, and G. Viesti, Phys. Rev. C **35**, 2125 (1987).

[20] J. L. Wile, W. U. Schroder, J. R. Huizenga, and D. Hilscher, Phys. Rev. C **35**, 1608 (1987).

[21] U. Gollerthan, H. G. Clerc, E. Hanelt, W. Morawek, V. Ninov, W. Schwab, K. H. Schmidt, F. P. Hessberger, G. Munzenberg, R. S. Simon, J. P. Dufour, and M. Montoya, Phys. Lett. B **201**, 206 (1988).

[22] R. Lacey, N. N. Ajitanand, J. M. Alexander, D. M. de Castro Rizzo, G. F. Peaslee, L. C. Vaz, M. Kaplan, M. Kildir, G. La Rana, D. J. Moses, W. E. Parker, D. Logan, M. S. Zisman, P. DeYoung, and L. Kowalski, Phys. Rev. C **37**, 2540 (1988).

[23] R. Lacey, N. N. Ajitanand, J. M. Alexander, D. M. de Castro Rizzo, G. F. Peaslee, L. C. Vaz, M. Kaplan, M. Kildir, G. La Rana, D. J. Moses, W. E. Parker, D. Logan, M. S. Zisman, P. DeYoung, and L. Kowalski, Phys. Rev. C **37**, 2561 (1988).

[24] J. O. Newton, D. J. Hinde, R. J. Charity, J. R. Leigh, J. J. M. Bokhorst, A. Chatterjee, G. S. Foote, and S. Ogaza, Nucl. Phys. **A483**, 126 (1988).

[25] G. F. Peaslee, N. N. Ajitanand, J. M. Alexander, D. Guerreau, R. Lacey, L. C. Vaz, M. Kaplan, M. Kildir, D. J. Moses, D. Logan, and M. S. Zisman, Phys. Rev. C **38**, 1730 (1988).

[26] G. F. Peaslee, N. N. Ajitanand, J. M. Alexander, R. Lacey, L. C. Vaz, M. Kaplan, M. Kildir, D. J. Moses, D. Logan, and M. S. Zisman, Phys. Rev. C **39**, 488 (1989).

[27] F. Terrasi, A. Brondi, G. La Rana, G. DeAngelis, A. D'Onofrio, R. Moro, E. Perillo, and M. Romano, Phys. Rev. C **40**, 742 (1989).

[28] P. A. DeYoung, C. J. Gelderloos, D. Kortering, J. Sarafa, K. Zienert, M. S. Gordon, B. J. Fineman, G. P. Gilfoyle, X. Lu, R. L. McGrath, D. M. de Castro Rizzo, J. M. Alexander, G. Auger, S. Kox, L. C. Vaz, C. Beck, D. J.

Henderson, D. G. Kovar, and M. F. Vineyard, Phys. Rev. C **41**, R1885 (1990).
[29] J. H. Lee, W. Benenson, and D. J. Morrissey, Phys. Rev. C **41**, 1562 (1990).
[30] R. J. Charity, K. X. Jing, D. R. Bowman, M. A. McMahan, G. J. Wozniak, L. G. Moretto, N. Colonna, G. Guarino, A. Pantaleo, L. Fiore, A. Gobbi, and K. D. Hildenbrand, Nucl. Phys. **A511**, 59 (1990).
[31] T. Ericson and V. Strutinski, Nucl. Phys. **8**, 284 (1958); **9**, 689 (1959).
[32] T. Ericson, Adv. Phys. **9**, 425 (1960).
[33] T. Dossing, Licentiat thesis, University of Copenhagen, Denmark, 1977.
[34] G. L. Catchen, M. Kaplan, J. M. Alexander, and M. F. Rivet, Phys. Rev. C **21**, 940 (1980).
[35] D. J. Moses, M. Kaplan, J. M. Alexander, D. Logan, M. Kildir, L. C. Vaz, N. N. Ajitanand, E. Duek, and M. S. Zisman, Z. Phys. A **320**, 229 (1985).
[36] M. Kaplan, DOE Annual Report No. COO-3246-25, Carnegie Mellon University, October 1985 (unpublished); also W. E. Parker, M. Kaplan, D. J. Moses, and R. J. Welberry, unpublished results.
[37] R. C. Reedy, M. J. Fluss, G. F. Herzog, L. Kowalski, and J. M. Miller, Phys. Rev. **188**, 1771 (1969).
[38] J. Galin, B. Gatty, D. Guerreau, C. Rousset, U. C. Schlotthauer-Voos, and X. Tarrago, Phys. Rev. C **9**, 1113 (1974).
[39] D. J. Moses, Ph.D. thesis, Carnegie Mellon University, 1986 (unpublished).
[40] D. J. Moses, M. Kaplan, M. Kildir, D. R. G. Logan, G. La Rana, W. E. Parker, R. Lacey, G. F. Peaslee, J. M. Alexander, N. N. Ajitanand, L. C. Vaz, and M. S. Zisman, Nucl. Phys. **A465**, 339 (1987).
[41] M. M. Fowler and R. C. Jared, Nucl. Instrum. Methods **124**, 341 (1975).
[42] H. Ikezoe, N. Shikazono, Y. Tomita, Y. Sugiyama, and K. Ideno, Nucl. Phys. **A462**, 150 (1987).
[43] H. Morgenstern, W. Bohne, K. Grabisch, H. Lehr, and W. Stoffler, Z. Phys. A **313**, 39 (1983).
[44] W. E. Parker, Ph.D. thesis, Carnegie Mellon University, 1989 (unpublished).
[45] N. N. Ajitanand, R. Lacey, G. F. Peaslee, E. Duek, and J. M. Alexander, Nucl. Instrum. Methods Phys. Res. **A243**, 111 (1986).
[46] P. Frobrich, Phys. Rep. **116**, 337 (1984).
[47] L. C. Vaz and J. M. Alexander, Z. Phys. A **318**, 231 (1984).
[48] Carnegie Mellon-Stony Brook Collaboration (unpublished).
[49] N. N. Ajitanand, G. La Rana, R. Lacey, D. J. Moses, L. C. Vaz, G. F. Peaslee, D. M. de Castro Rizzo, M. Kaplan, and J. M. Alexander, Phys. Rev. C **34**, 877 (1986).
[50] J. M. Alexander, D. Guerreau, and L. C. Vaz, Z. Phys. A **305**, 313 (1982).
[51] G. La Rana, D. J. Moses, W. E. Parker, M. Kaplan, D. Logan, R. Lacey, J. M. Alexander, and R. J. Welberry, Phys. Rev. C **35**, 373 (1987).
[52] R. Lacey, N. N. Ajitanand, J. M. Alexander, D. M. de Castro Rizzo, P. DeYoung, M. Kaplan, L. Kowalski, G. La Rana, D. Logan, D. J. Moses, W. E. Parker, G. F. Peaslee, and L. C. Vaz, Phys. Lett. B **191**, 253 (1987).
[53] D. J. Moses, M. Kaplan, G. La Rana, W. E. Parker, R. Lacey, and J. M. Alexander, Phys. Rev. C **36**, 422 (1987).
[54] G. La Rana, R. Moro, A. Brondi, P. Cuzzocrea, A. D'Onofrio, E. Perillo, M. Romano, F. Terrasi, and E. Vardaci, Phys. Rev. C **37**, 1920 (1988).
[55] B. Fornal, G. Viesti, G. Nebbia, G. Prete, and J. B. Natowitz, Phys. Rev. C **40**, 664 (1989).
[56] B. Fornal, F. Gramegna, G. Prete, G. Nebbia, R. Smith, G. D'Erasmo, L. Fiore, A. Pantaleo, G. Viesti, P. Blasi, F. Lucarelli, I. Iori, and A. Moroni, Phys. Rev. C **41**, 127 (1990).
[57] B. Fornal, F. Gramegna, F. Prete, G. D'Erasmo, E. M. Fiore, L. Fiore, A. Pantaleo, V. Paticchio, G. Viesti, P. Blasi, F. Lucarelli, M. Anghinolfi, P. Corvisiero, M. Taiuti, A. Zucchiatti, P. F. Bortignon, Ch. Ferrer, G. Nardelli, and G. Nebbia, Phys. Rev. C **42**, 1472 (1990).
[58] H. Ikezoe, N. Shikazono, Y. Nagame, Y. Sugiyama, Y. Tomita, K. Ideno, A. Iwamoto, and T. Ohtsuki, Phys. Rev. C **42**, 342 (1990).
[59] H. Ikezoe, N. Shikazano, Y. Nagame, Y. Sugiyama, Y. Tomita, K. Ideno, A. Iwamoto, and T. Ohtsuki, Phys. Rev. C **42**, R1187 (1990).
[60] U. Gollerthan, T. Brohm, H. G. Clerc, E. Hanelt, M. Horz, W. Morawek, W. Schwab, K. H. Schmidt, F. P. Hessberger, G. Munzenberg, V. Ninov, R. S. Simon, J. P. Dufour, and M. Montoya, Z. Phys. A **338**, 51 (1991).
[61] M. Kaplan, W. E. Parker, D. J. Moses, G. La Rana, R. J. Welberry, D. Logan, R. Lacey, J. M. Alexander, D. M. de Castro Rizzo, and P. DeYoung, in *Proceedings of the Texas A&M Symposium on Hot Nuclei, College Station, 1987,* edited by S. Schlomo, R. P. Schmitt, and J. B. Natowitz (World Scientific, Singapore, 1988), p. 115.
[62] J. M. Alexander, G. Auger, M. Kaplan, L. Kowalski, R. Lacey, G. La Rana, M. T. Magda, and G. F. Peaslee, in *Proceedings of the Symposium on Nuclear Dynamics and Nuclear Disassembly, Dallas, 1989,* edited by J. B. Natowitz (World Scientific, Singapore, 1989), p. 211.
[63] The code LILITA__N90 is an extensively modified version of the LILITA program originally developed by J. Gomez del Campo (Ref. [64]). It has been renamed to differentiate it from several other versions of LILITA.
[64] J. Gomez del Campo and R. G. Stokstad, Oak Ridge National Laboratory Report ORNL TM-7295, 1981; J. Gomez del Campo, R. G. Stokstad, J. A. Biggerstaff, R. A. Dayras, A. H. Snell, and P. H. Stelson, Phys. Rev. C **19**, 2170 (1979).
[65] G. La Rana, R. Moro, A. Brondi, P. Cuzzocrea, A. D'Onofrio, E. Perillo, M. Romano, and F. Terrasi, Nucl. Phys. **A488**, 211c (1988).
[66] J. R. Grover and J. Gilat, Phys. Rev. **157**, 802 (1967).
[67] I. M. Govil, J. R. Huizenga, W. U. Schroder, and J. Toke, Phys. Lett. B **197**, 515 (1987).
[68] V. V. Pashkevich, Nucl. Phys. **A169**, 275 (1971).
[69] L. Schad, H. Ho, G.-Y. Fan, B. Lindl, A. Pfoh, R. Wolski, and J. P. Wurm, Z. Phys. A **318**, 179 (1984).
[70] A. Brucker, B. Lindl, M. Bantel, H. Ho, R. Muffler, L. Schad, M. G. Trauth, and J. P. Wurm, Phys. Lett. B **206**, 13 (1988).
[71] D. J. Hinde, H. Ogata, M. Tanaka, T. Shimoda, N. Takahashi, A. Shinohara, S. Wakamatsu, K. Katori, and H. Okamura, Phys. Rev. C **37**, 2923 (1988).
[72] N. G. Nicolis, D. G. Sarantites, L. A. Adler, F. A. Dilmanian, K. Honkanen, Z. Majka, L. G. Sobotka, Z. Li, T. M. Semkow, J. R. Beene, M. L. Halbert, D. C. Hensley, J. B. Natowitz, R. P. Schmitt, D. Fabris, G. Nebbia, and G. Mouchaty, Phys. Rev. C **41**, 2118 (1990).
[73] S. Cohen, F. Plasil, and W. J. Swiatecki, Ann. Phys. (N.Y.) **82**, 557 (1974).

[74] M. G. Mustafa, P. A. Baisden, and H. Chandra, Phys. Rev. C **25**, 2524 (1982).

[75] A. J. Sierk, Phys. Rev. C **33**, 2029 (1986).

[76] J. J. Kolata, R. A. Kryger, P. A. DeYoung, and F. W. Prosser, Phys. Rev. Lett. **61**, 1178 (1988).

[77] E. Tomasi, X. S. Chen, S. Leray, C. Ngo, M. Barranco, X. Vinas, and H. Ngo, Nucl. Phys. **A389**, 69 (1982).

[78] X. S. Chen, C. Ngo, and E. Tomasi, Nucl. Phys. **A401**, 143 (1983).

[79] G. Batko and O. Civitarese, Phys. Rev. C **37**, 2647 (1988).

[80] G. Bozzolo and J. P. Vary, Phys. Rev. C **31**, 1909 (1985).

[81] G. Bozzolo, O. Civitarese, and J. P. Vary, Phys. Rev. C **37**, 1240 (1988).

[82] L. C. Vaz, D. Logan, J. M. Alexander, E. Duek, D. Guerreau, L. Kowalski, M. F. Rivet, and M. S. Zisman, Z. Phys. A **311**, 89 (1983).

[83] N. Carjan and J. M. Alexander, Phys. Rev. C **38**, 1692 (1988).

[84] J. Boger, S. Kox, G. Auger, J. M. Alexander, A. Narayanan, M. A. McMahan, D. J. Moses, M. Kaplan, and G. P. Gilfoyle, Phys. Rev. C **41**, R801 (1990).

[85] Y. Nagame, H. Ikezoe, S. Baba, K. Hata, T. Sekine, S. Ichikawa, M. Magara, K. Ideno, A. Yokoyama, Y. Hatsukawa, and T. Ohtsuki, Nucl. Phys. **A510**, 518 (1990).

[86] Some preliminary results of the work described here have been given in Ref. [36] above.

[87] B. Fornal, G. Prete, G. Nebbia, F. Trotti, G. Viesti, D. Fabris, K. Hagel, and J. B. Natowitz, Phys. Rev. C **37**, 2624 (1988).

[88] G. Viesti, B. Fornal, D. Fabris, K. Hagel, J. B. Natowitz, G. Nebbia, G. Prete, and F. Trotti, Phys. Rev. C **38**, 2640 (1988).

[89] M. Gonin, L. Cooke, K. Hagel, Y. Lou, J. B. Natowitz, R. P. Schmitt, B. Srivastava, W. Turmel, H. Utsunomiya, R. Wada, B. Fornal, G. Nardelli, G. Nebbia, G. Viesti, R. Zanon, G. Prete, P. Gonthier, and B. Wilkins, Phys. Lett. B **217**, 406 (1989).

[90] J. R. Huizenga, A. N. Behkami, I. M. Govil, W. U. Schroder, and J. Toke, Phys. Rev. C **40**, 668 (1989).

[91] G. Viesti, M. Anghinolfi, P. F. Bortignon, P. Corvisiero, L. Djilavian, B. Fornal, F. Gramegna, J. B. Natowitz, G. Nebbia, G. Prete, M. Taiuti, and A. Zucchiatti, Phys. Rev. C **40**, R1570 (1989).

[92] S. Shlomo and J. B. Natowitz, Phys. Lett. B **252**, 187 (1990).

[93] M. Gonin, L. Cooke, K. Hagel, Y. Lou, J. B. Natowitz, R. P. Schmitt, S. Shlomo, B. Srivastava, W. Turmel, H. Utsunomiya, R. Wada, G. Nardelli, G. Nebbia, G. Viesti, R. Zanon, B. Fornal, G. Prete, K. Niita, S. Hannuschke, P. Gonthier, and B. Wilkins, Phys. Rev. C **42**, 2125 (1990).

[94] A. Chbihi, L. G. Sobotka, N. G. Nicolis, D. G. Sarantites, D. W. Stracener, Z. Majka, D. C. Hensley, J. R. Beene, and M. L. Halbert, Phys. Rev. C **43**, 666 (1991).